Cement and Concrete Research 177 (2024) 107419

Contents lists available at ScienceDirect

Cement and Concrete Research

journal homepage: www.elsevier.com/locate/cemconres

Characterisation of iron-rich cementitious materials

Aniruddha Baral [a,*], Cecilia Pesce [a], Antonia S. Yorkshire [a], Zhanar Zhakiyeva [a,b], Ruben Snellings [c,d], Theodore Hanein [a,e,*], John L. Provis [a,f], Arne Peys [g,*]

[a] Department of Materials Science and Engineering, The University of Sheffield, S1 3JD, United Kingdom
[b] Department of Chemical and Materials Engineering, School of Engineering and Digital Sciences, Nazarbayev University, Kabanbay Batyr Ave. 53, Astana 010000, Kazakhstan
[c] Department of Earth and Environmental Sciences, KU Leuven, Celestijnenlaan 200 E, 3001 Leuven, Belgium
[d] Department of Materials Engineering, KU Leuven, Kasteelpark 44/2450, 3001 Leuven, Belgium
[e] Manatee Consulting Limited, Sheffield S3 7XL, United Kingdom
[f] Paul Scherrer Institut, Laboratory for Waste Management, Forschungsstrasse 111, 5232 Villigen PSI, Switzerland
[g] Sustainable Materials, VITO, Boeretang 200, 2400 Mol, Belgium

ARTICLE INFO

Keywords:
Cement
Ferrite
Supplementary cementitious materials
Clinker
X-ray
Spectroscopy

ABSTRACT

Iron is the fourth most abundant element in the Earth's crust, and cementitious materials are expected to contain iron-bearing phases, either in major or minor quantities. Iron-rich cement clinker is gaining attention because of its lower carbon footprint and higher sulfate resistance, while iron-rich resources are also increasingly being investigated as supplementary cementitious materials or as precursors for alkali-activated materials. However, iron-containing phases are among the least characterised in cementitious materials. This review paper discusses challenges in the characterisation of iron-containing phases for i) routinely used characterisation techniques, ii) specific characterisation techniques that excel at characterising iron-bearing phases, and proposes future areas of research to improve the accuracy and usability of these techniques. Micro-absorption, high X-ray and neutron scattering cross-section, fluorescence, and paramagnetism of iron can affect the application of X-ray diffraction, pair distribution function analysis, small-angle X-ray scattering, Raman spectroscopy, and nuclear magnetic resonance spectroscopy. X-ray absorption near-edge structure, extended X-ray absorption fine structure, ^{57}Fe Mössbauer spectroscopy, and electron paramagnetic resonance spectroscopy are particularly suitable for characterising the iron oxidation states and local bonding environment in the iron-containing phases. UV–Visible spectroscopy, ion chromatography, and titration methods can be potentially used to quantify iron concentration and oxidation states in aqueous solution, but further research is required to apply them in the field of cementitious materials.

1. Introduction

Cementitious materials are produced from common primary resources and industrial residues that often contain significant amounts of iron [1]. As a result, many hardened cements will contain different Fe-containing phases derived from the raw materials, and/or incorporate Fe within their reaction products. Moreover, cements containing high amounts of calcium aluminoferrite ($Ca_2(Al_xFe_{2-x})O_5$, with $0 \leq x \leq 1.34$) are gaining attention, as their production involves less energy consumption and CO_2 emissions compared to Portland cement (PC) due to the lower calcium content and reduced clinkering temperature. Additionally, ferrite-rich cements provide better resistance against sulfate attack [2–4]. Despite this, Fe-rich cement components are the least characterised and understood parts of common cements, in terms of their chemistry and effects on cement microstructure. Their role in the hydration and performance of cements is therefore less clear than for other components. Some of the main Fe-bearing phases commonly encountered in cement precursors and consolidated binder systems are identified in Table 1.

The raw materials used to produce PC clinker are conventionally limestone, clays, shale and minor corrective additives [5]. In the clinkering process, Fe oxides combine with Ca and Al to form the ferrite phase $Ca_2(Al_xFe_{2-x})O_5$. The high-temperature $CaO\text{-}Al_2O_3\text{-}Fe_2O_3$ phase diagram is well-defined in the literature [6–8]. Fe is partly soluble in

* Corresponding author.
E-mail addresses: a.baral@sheffield.ac.uk (A. Baral), t.hanein@sheffield.ac.uk (T. Hanein), arne.peys@vito.be (A. Peys).

https://doi.org/10.1016/j.cemconres.2023.107419
Received 12 July 2023; Received in revised form 6 December 2023; Accepted 31 December 2023
Available online 18 January 2024

Table 1
Fe-containing phases commonly reported in the literature.

	Phase(s)	Occurrences
Clinker phases	Ferrite ($Ca_2Al_xFe_{2-x}O_5$) Fe/Al-substituted ye'elimite ($Ca_4(AlO_2)_6SO_4$) Fe oxides:	Portland clinker phase. Natural analogues occur as the brownmillerite mineral. Calcium sulfoaluminate clinker phase
	• Hematite (Fe_2O_3) • Maghemite (Fe_2O_3) • Magnetite (Fe_3O_4) • Wüstite (~FeO) • Spinel compounds ($ZnFe_2O_4$, $FeAl_2O_4$, $FeCr_2O_4$, Fe_3O_4 etc.)	Minor or trace components (or largely unreactive) in traditional cementitious by-products such as blast-furnace slag and fly ash, but also present in other Fe-rich by-products/residues (bauxite residue, fayalitic slag, zinc production sludges, water treatment sludge). Trace amount of Fe-oxides may originate if using steel grinding equipment; zirconia or agate grinding jars and balls are recommended to avoid this.
	Goethite (α-FeOOH)	Significant quantities in hydrometallurgical by-products (bauxite residue, zinc production sludges, water treatment sludge)
	Fe-containing silicates:	
Phases in raw materials (for clinkers, SCM, or AAM)	• Fayalite (Fe_2SiO_4) • Hedenbergite ($CaFeSi_2O_6$) • Augite ((Ca,Na)(Mg,Fe,Al,Ti)(Si,Al)$_2O_6$) • Ferrosilite ($FeSiO_3$)	Naturally occurring minerals or present in fayalitic slags.
	Fe-containing silicate glass	The main phase of rapidly cooled fayalitic slags; present in coal fly ashes, volcanic ashes and quenched steel slag.
	Fe-sulfides	
	• Pyrite and marcasite (FeS_2) • Pentlandite ($(Fe,Ni)_9S_8$) • Pyrrhotite ($Fe_{1-x}S$)	Present in non-ferrous metal mine tailings, also found in water treatment sludge, clays or dredged sediments and as inclusions in metallurgical slags
	Metallic iron (Fe(0))	Inclusions in ferrous slags (blast furnace slag or steel slag). Structural reinforcement in concrete (not discussed here).
	Fe(III)/Al-substituted hydrate phases[a]:	
Hydrate phases	• Fe-AFm (various); e.g., $C_4(A,F)\$H_{12}$ • Fe-ettringite; $C_6(A,F)\$_3H_{32}$ • Fe-hydrogarnet; $C_3(A,F)H_6$ • Amorphous silicate network; N-(A,F)-S-H	Formed as a result of Fe substitution into Al sites of hydrate phases.
	Fe(II)-containing hydrates/hydroxides:	
	• Layered double hydroxides • Trioctahedral phyllosilicates	May form as a result of the hydration of Fe (II) in Portland cement or alkali-activated systems

[a] Hydrated phases are defined in cement chemistry abbreviated notation, where C = CaO (etc.)

almost all calcium aluminate phases, and Al is partly soluble in all calcium iron oxide phases. In PC clinker, the ferrite phase generally exists as a solid solution of $Ca_2(Al_xFe_{2-x})O_5$, with x varying between 0 and 1.34, along with substitution of Fe^{3+} by ions including Mg^{2+}, Si^{4+}, Ti^{4+} and others. [9]. In calcium sulfoaluminate (C$A) clinkers, Fe can substitute for Al in ye'elimite, $Ca_4Al_{(6-2y)}Fe_{2y}SO_{16}$, with $0 \leq y \leq 1.5$, depending on the iron content of the clinker [10]. At extremely high iron content (with excess Fe beyond what is required to reach y = 1.5), srebrodolskite ($Ca_2Fe_2O_5$) and anhydrite ($CaSO_4$) form instead of ye'elimite. The Al/Fe ratios in ferrite and ye'elimite phases affect both the manufacturing process and the performance of the clinker in cement, with the melting point, grindability, and dissolution and hydration rates increasing with an increase in Al/Fe ratio [11–13]. Upon hydration of clinkers with dissolution of Fe-bearing phases, Fe is incorporated into a range of hydration products, such as ettringite (AFt phases), layered double hydroxides (e.g., AFm phases), hydrogarnets, or Fe hydroxides [14–16]. There is, however, some debate about the extent of Fe incorporation into C-S-H, AFt and AFm phases [1].

Cements that are produced using industrial by-products such as blast-furnace slag (BFS; from pig-iron production) or fly ashes (FA; from coal-burning operations) as supplementary cementitious materials or precursors may contain entrained metallic or oxidic Fe particles, which are considered to be largely unreactive during hydration [1,17,18]. Other Fe-rich raw materials, such as smectite clays, volcanic ashes, steel slags, fayalitic slags, or vitrified bauxite residue can contribute a substantial amount of reactive iron to the cementitious system [1]. This also results in a substantial incorporation of iron in the hydrates or other binding phases. Substantial involvement of iron can also take place in a Fe-rich layered double hydroxide (LDH) phase [19], nanocrystalline trioctahedral Fe^{2+}-containing phyllosilicates [20] resembling the magnesium silicate hydrate described by Bernard et al. [21], and/or a Fe^{3+}-containing silicate network [22].

The characterisation of Fe-bearing phases both before and after hardening is fundamental to understanding the role of iron in cementitious materials. When characterising Fe-containing cementitious materials, the necessary sample preparation techniques mostly follow the same guidelines as regular cementitious materials [23]. However, additional care needs to be taken especially when performing mineral identification or characterising speciation of Fe in the sample to avoid the oxidation of Fe^{2+} to Fe^{3+} when exposing ground samples to ambient air or elevated temperature, as Fe^{2+}-containing phases can be more rapidly oxidized in comparison with the rate of decomposition of common cementitious phases and the rate of oxidation is not much affected by hydration stoppage. This has been found to be particularly important for the characterisation of Fe-rich alkali-activated materials (AAMs) [24] and may have important implications for the interpretation of the molecular structure of AAMs [25–27].

In this review, we discuss standard and advanced analytical techniques used to characterise cementitious materials and their application to Fe-bearing cementitious phases. Surface-sensitive analysis techniques that are specifically relevant to steel-concrete interface characterisation, rather than the cementitious phases, have not been discussed in this paper. Understanding of the Fe-bearing minerals found in raw materials and precursors utilised for manufacturing of cementitious materials with

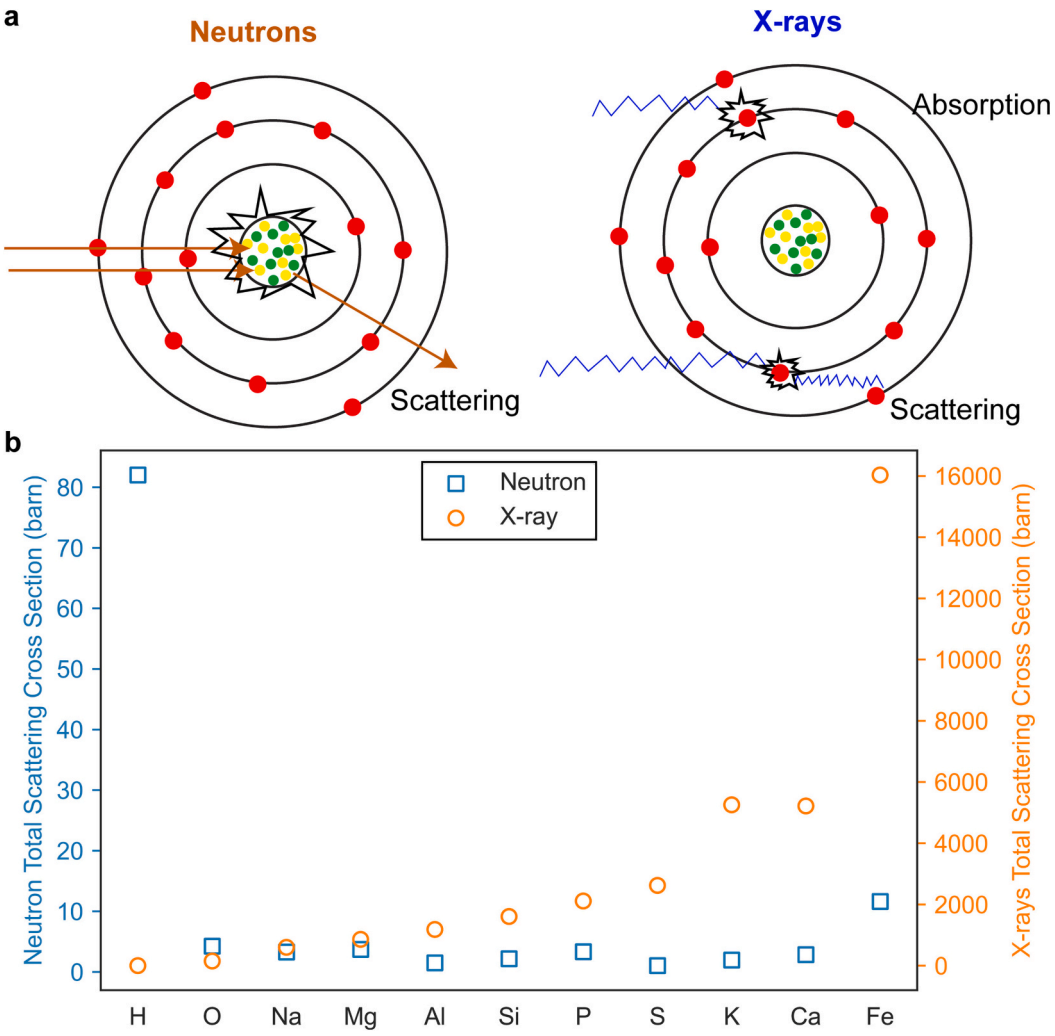

Fig. 1. Interaction of neutrons and X-rays with an atom (a). The total scattering cross-sections for neutrons and X-rays (10 keV) for elements commonly found in cementitious materials are shown in (b).[+] The X-ray cross-section increases with atomic number, whereas the neutron-scattering cross-section is not directly linked to the atomic number.
[+]1 barn = 10^{-28} m^2.

high iron content is also of importance. In view of this, and the many different non-conventional Fe-containing raw materials such as steel slag, bauxite residue and fayalitic slags that can be utilised for cementitious materials production [1], this paper will provide an overview of a range of techniques for characterising a wide variety of Fe-bearing phases. We focus on challenges posed to these techniques specifically by Fe-rich phases, and modifications that can or must be made for in-depth characterisation of Fe-bearing cements.

2. Characterisation by X-ray and neutron scattering

X-rays are high-energy electromagnetic waves that interact with the electrons of atoms, while neutrons are subatomic particles that interact with the nuclei of atoms via short-range nuclear forces (Fig. 1a). Many analytical techniques have been developed using both X-rays and neutrons for a range of applications with relevance to characterisation of cementitious materials, and several of these are strongly influenced by the presence of iron in the cements.

Scattering experiments are used for the qualitative identification and characterisation of individual phases within cementitious materials, as well as the quantification of their abundances [28]. Three complementary methods are discussed here: X-ray and neutron powder diffraction analysis which mainly concern the characterisation and quantification of crystalline phases; pair distribution function (PDF) analysis that can provide additional structural information for disordered or non-crystalline solids; and small-angle X-ray scattering (SAXS) and small-angle neutron scattering (SANS) that can provide structural information at the nanoscale for porosity measurements, including determination of surface area. X-ray diffraction (XRD) and X-ray PDF (XPDF) are versatile and widely used techniques. Powder neutron diffraction (PND) and neutron PDF (NPDF) methods are generally somewhat less accessible than X-ray techniques due to the need for a specialised neutron source facility but are nonetheless frequently used in tandem with XRD and XPDF to provide accurate structural information, or to address problems where X-rays cannot give the necessary sensitivity.

2.1. X-ray powder diffraction

X-ray powder diffraction is a widely used technique as XRD instruments are readily accessible in many material science laboratories. Sample preparation, data collection and analysis are relatively straightforward but can be time-consuming. General guidelines regarding XRD measurement and analysis can be found elsewhere [28]. Here, particular aspects related to the analysis of Fe-rich cementitious materials are highlighted.

Most laboratory diffractometers use a Cu X-ray source. As the Cu Kα

wavelength is close to the Fe Kα absorption edge, a relatively strong X-ray fluorescence effect is observed for Fe-rich materials leading to high background and low signal-to-noise ratios. The fluorescence effect can be mitigated by monochromator optics, although this comes at the expense of signal intensity loss. For quantitative phase analysis of Fe-rich materials, it is important to reduce interference from micro-absorption effects. This effect originates from X-ray absorption contrasts among different phases in multi-phase mixtures, e.g., Fe_2O_3 (220.8 cm^2/g) and SiO_2 (34.8 cm^2/g), in the case of commonly used Cu Kα radiation (1.5406 Å or 8.048 keV). Micro-absorption effects can be mitigated by finer grinding of the sample (to 2–3 μm), or by selecting a different X-ray source energy to avoid having absorption edges falling between the elements of interest. For instance, the use of Co Kα radiation (1.7902 Å or 6.926 keV) removes the absorption contrast between Fe_2O_3 (46.8 cm^2/g) and SiO_2 (53.0 cm^2/g), and also brings benefit by reducing the fluorescence effects mentioned above, because the Co Kα wavelength is not so close to the Fe absorption edge.

The interpretation of the collected XRD data is facilitated by analysis software packages. The phase identification and quantification routines in these programs rely on phase and profile databases. General purpose databases, such as powder diffraction files published by the International Centre for Diffraction Data (ICDD) or the Inorganic Crystal Structures Database (ICSD) [28], the American Mineralogist Crystal Structure Database [29], and the Crystallography Open Database (COD) [30] contain indexed diffraction patterns and crystal structures for assignment of Fe oxides or other Fe-bearing mineral phases (see Table 2). These databases can report numerous entries for the same phase. Pre-selection of relevant and reliable patterns and structures is an important aid in reaching consistent and relevant results.

XRD quantitative phase analysis (QPA) of cementitious materials can be routinely carried out following the Rietveld method [39]. The Rietveld method is based on calculation of diffraction patterns from fundamental crystal structure properties combined with peak shape functions. The analysis is based on the fitting of the calculated pattern to the measured data by refinement of a selection of crystal structure and peak shape parameters. The refined parameters routinely include phase scale factors and crystal lattice parameters. The scale factors are recalculated into phase mass fractions, while the refined lattice parameters can provide indications of isostructural substitution in the lattice [40].

In regular Rietveld QPA, only the included phases are taken into account and their sum is constrained to 100 %. Unidentified, non-fitted, or amorphous phases are excluded. As many cementitious materials contain a significant fraction of amorphous phase(s), internal and external standard methods can be implemented to allow quantification of the weight fraction of the amorphous content, relative to the identified phases.

Selecting appropriate crystal structures to describe the identified phases is particularly important as a starting point for Rietveld QPA. Reported crystal structures may not include all required information or may be derived from data collected at high temperatures or pressures. In addition, site occupancies for solid solution series (e.g. Al—Fe in ferrite) can differ slightly between different crystal structure models and the selection of matching models will improve the accuracy of the QPA [28].

As mentioned above, the QPA of Fe-rich phases may be biased by micro-absorption effects. To some extent, this can be corrected by applying a Brindley correction [41], although this requires a median particle size diameter to be known. In the case of ferrite quantification in Portland cement, this can result in relatively minor changes (around 0.5 wt%) in phase abundancies [42]. Refinement of lattice parameters can provide insights into phase composition, as exemplified in Fig. 2 for ferrite where a monotonic reduction of lattice parameter dimensions and unit cell volume is observed for increasing Al content. Furthermore, an increase in x to values above 0.56 in $Ca_2Fe_{2-x}Al_xO_5$ changes the space group symmetry from Pnma to I2mb.

Alternatively, the atomic site occupancies may be refined to determine Fe:Al substitution levels. As Fe usually is the significantly heavier element in cement phase solid solutions, the contrast in X-ray scattering factor with the other solid solution members (e.g., Al or Mg) could allow refinement for major phases in the absence of significant peak overlap. As this situation is uncommon in cements, it has been noted that conventional laboratory-based powder XRD techniques may not have sufficient resolution for refining Fe:Al ratios [43]. Thus, higher-specification diffractometers or synchrotron X-ray sources may be useful for such in-depth analyses. For instance, Dilnesa et al. [44] carried out Rietveld refinement on synthesised Fe-Si-hydrogarnet phases to investigate the existence of solid-solution series within CaO-Al_2O_3-Fe_2O_3-H_2O systems, with diffraction patterns measured using synchrotron X-rays ($\lambda = 0.697751$ Å), and were able to calculate the structure parameters of two types of hydroandradites ($Ca_3Fe_2(SiO_4)_y(OH)_{4(3-y)}$; $0 < y < 3$) present in the Fe-Si-hydrogarnet samples.

Table 2
Example references for diffraction data of Fe-containing phases contained in ICSD, as reported by [28].

Mineral phase	Cement nomenclature (if applicable)	Reference
Hematite (Fe_2O_3)		[31]
Magnetite (Fe_3O_4)		[32]
Wüstite (~FeO)		[33]
Magnesioferrite ($MgFe_2O_4$)		[34]
Ferrite/Brownmillerite ($Ca_2Al_xFe_{2-x}O_5$)	C_4AF	[35]
Srebrodolskite ($Ca_2Fe_2O_5$)	C_2F	[35]
Fe-AFm ($Ca_4Fe_2(OH)_{12}(X)(H_2O)_{-6}$ where $X = CO_3$ or SO_4)	$C_4(A,F)\$H_{12}$	[36,37]
Fe-hydrogarnet ($Ca_3Fe_2(SiO_4)_{2.16}(OH)_{3.36}$)	$C_3(A,F)H_6$	[36]
Fe-ettringite ($Ca_6Fe_2(SO_4)_3(OH)_{12}(H_2O)_{26}$)	$C_6(A,F)\$_3H_{32}$	[38]

2.2. Powder neutron diffraction

Powder neutron diffraction (PND) is often used as a complementary method together with XRD as a combined refinement approach. The advantages of using PND in conjunction with XRD are several: (i) the scattering cross sections vary randomly across the periodic table, unlike X-ray cross-sections that rise steadily with increasing atomic number (Fig. 1b); (ii) different isotopes of the same elements have different cross sections, which can enable measurements using isotopic substitution (e.g., substitution of ^1H by ^2H (also abbreviated D)); and (iii) most light elements, including hydrogen, scatter neutrons relatively strongly compared to their weak interactions with X-rays. Applying both X-ray and neutron diffraction techniques also results in better structure refinement. However, the intrinsic limitations of neutron techniques, such as the need for a neutron source, and the generally low signal-to-noise ratio achieved because neutron detection at high spatial resolution is relatively difficult, hinders PND from becoming a routine technique.

PND has been mostly used in the cementitious materials field for characterising water environments; a summary of the utilisation of PND in the cementitious materials field, as well as PND test methods, are provided as Supporting Information. PND has also been applied to iron-containing cementitious phases when the properties of their constituent elements can be exploited. Comparative Rietveld analysis with both synchrotron XRD and PND has been used to quantify cement clinker phases, including tetracalcium aluminoferrite at varying Al/Fe ratios [49]. Simultaneous Rietveld refinement of X-ray and neutron diffraction data has also been used for accurate structural analysis of MgO-doped brownmillerite - $Ca_2Fe_{0.95}Al_{0.95}Mg_{0.05}Si_{0.05}O_5$ [50].

2.3. Pair distribution function analysis

The short-range order (e.g., <4 nm) of nanocrystalline, disordered, and glassy materials can be revealed using X-ray or neutron total scattering experiments and pair distribution function (PDF) analysis. The

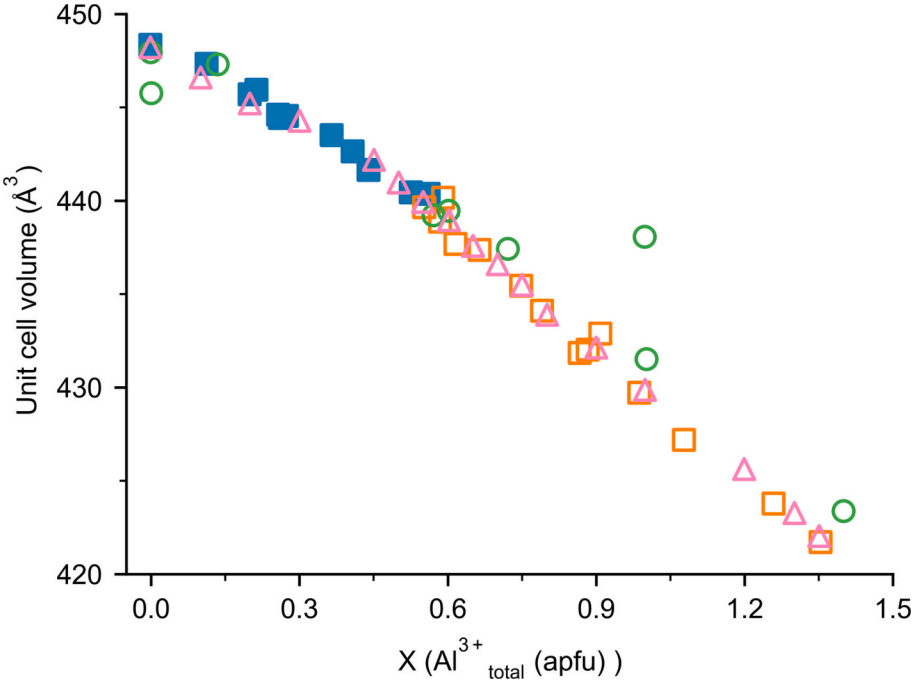

Fig. 2. Decrease in ferrite (brownmillerite) unit cell volume with Al substitution level (X) in $Ca_2Fe_{2-x}Al_xO_5$ solid solution (replotted from Redhammer et al. [35]). $Ca_2Fe_{2-x}Al_xO_5$ has space group symmetry Pnma (x < 0.56 atoms per formula unit (apfu)), which changes to I2mb symmetry at higher aluminium content (x > 0.56 apfu). The hollow and filled markers represent samples with I2mb and Pnma space group symmetry, respectively. The rectangles represent samples synthesised at 1500 °C, and hollow triangles represent data from samples synthesised at 1300 °C. The circles are data from previous work [45–48].

scattered intensity I is proportional to the structure factor, $S(\boldsymbol{Q})$, where $\boldsymbol{Q}$ is the scattering vector. Fourier transformation of the structure factor yields the real space partial PDF, $g(r)$. This last function defines the probability of finding an atom β at a distance r from an atom α (and equally α from β) as in Eq. (1):

$$g_{\alpha\beta}(r) = 1 + \frac{1}{2\pi^2\rho_n}\int_0^\infty \left[S_{\alpha\beta}(Q) - 1\right] Q^2 \frac{sinQr}{Qr}\, dQ \qquad (1)$$

where ρ_n is the atomic number density (number of atoms per volume of the unit cell, $Å^{-3}$).[1]

The preparation and measurement principles of the X-ray/neutron total scattering experiments preceding PDF analysis are barely influenced by the presence of iron [52,53]. The complexity introduced by iron species in PDF interpretation is caused by two properties of iron: (i) it has a high scattering cross section in comparison with other elements in cementitious materials for both X-rays and neutrons; and (ii) the variability of the oxidation state and coordination number of iron causes a continuous spectrum of potential atomic correlations, rendering the fitting severely under-constrained [54,55].

Fig. 1b shows that atomic correlations involving iron will contribute particularly strongly to the X-ray PDF, and also (but maybe less markedly) to the neutron PDF. This not only causes the first Fe—O correlation peak to be more intense than would be expected simply from the relevant atomic ratios, but can also result in hiding cation-cation correlations between other elements as they may be masked by Fe-cation correlations [46]. This predominance of Fe signals can be beneficial in determining the role of iron in cementitious materials, but it hinders obtaining information on the other elements. However, even for the Fe signals the cation-cation correlations are tedious to attribute due to the large varieties of potential bond lengths and configurations. The generation of difference plots during in-situ testing and comparison with known crystalline structures might become necessary to extract valuable information (Fig. 3).

Variation of the oxidation state and coordination number of iron results in a change of the distance or bond length between the iron and oxygen atoms. Hence, in pure substances, the oxidation state and coordination number can be derived from the distance of the Fe—O correlation in the PDF. If iron is present in more than one phase or environment, this becomes challenging. If a crystalline phase is present, subtraction of a simulated PDF calculated from a structure file can help to isolate the signal of the disordered phases of interest. Theoretically, the average coordination number can be derived from the integral area of the first Fe—O correlation peak in the normalised PDF. To derive this from experimental results is tedious and leads to imprecise outcomes [25], even for synthetic iron silicate glasses. When using molecular dynamics (MD) to render a structure that fits with the PDF, the distribution of different coordination environments can be exactly computed. However, considering these results as the absolute truth requires trust in the accuracy of the force field and assumptions in the MD calculations, and the calculation of a one-dimensional PDF from a three-dimensional MD simulation may lead to a certain degree of ambiguity as there is not a one-to-one mapping between structure and PDF. Obtaining information on the oxidation state and coordination number from complementary characterisation techniques is recommended, e.g., from X-ray absorption (Section 4) or Mössbauer spectroscopy (Section 3.1).

Due to its advantages for characterising glassy and nano-crystalline structures, the most important applications for PDF analysis in Fe-rich cements to date have been in the characterisation of glassy (quenched) metallurgical slags – or their synthetic analogues – and their reaction products. Specifically for Fe-rich materials, the characterisation of quenched fayalitic slags/glasses and alkali-activated fayalitic slags/glasses has received breakthroughs from PDF analyses [25,56–59]. For example, Peys et al. [56] studied the alkali-activation of slags (Fig. 3)

[1] *In Eq. (1), the integral is taken over the whole Q-space, from zero to infinity. However, in a real diffraction experiment, the Q is limited, and the integral is taken from zero to Q_{max} leading to broader peaks and non-physical oscillations in $g(r)$. There are various ways to correct for limited Q_{max}, such as using a window function (e.g., Lorch function)* [51].

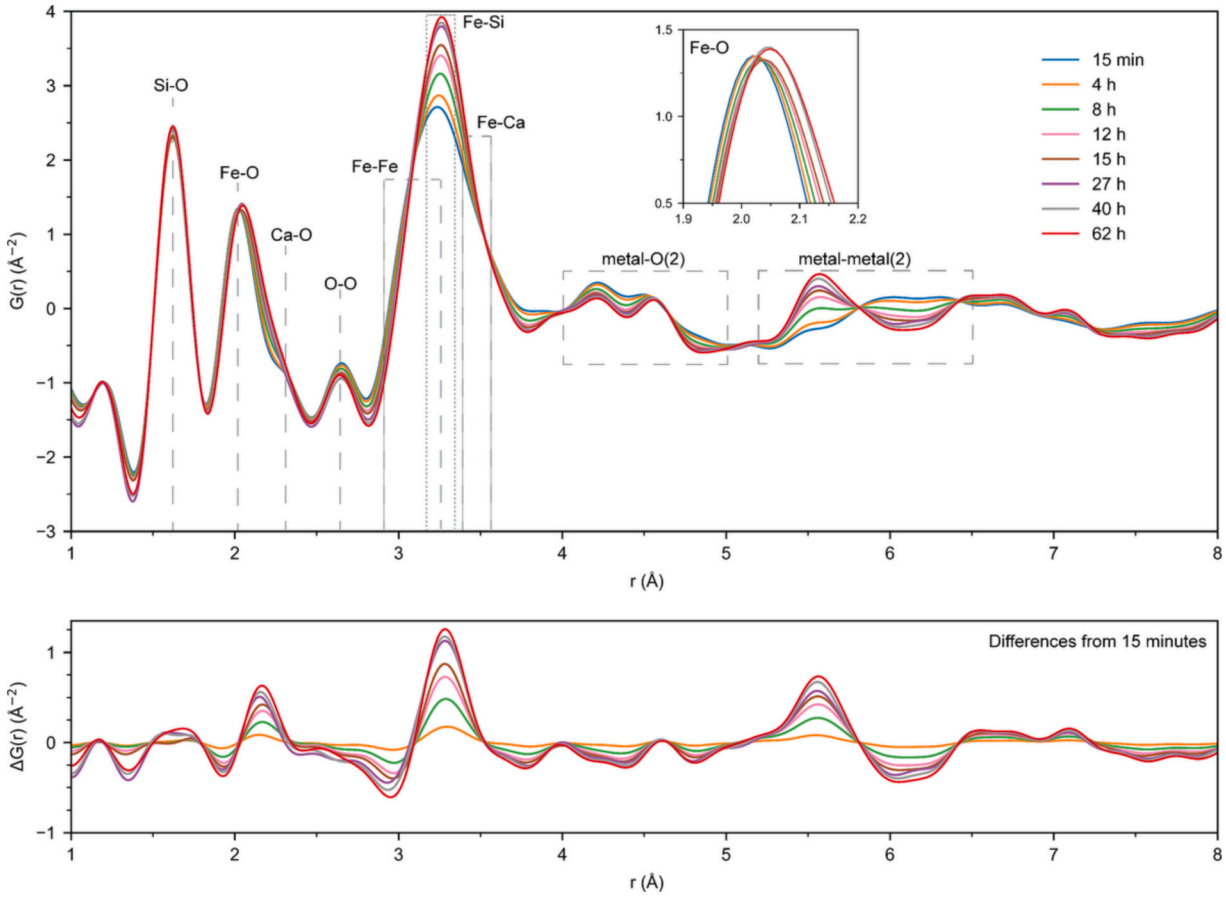

Fig. 3. Evolution of X-ray PDFs of sodium silicate-activated low-calcium slags during the first 62 h of reaction (replotted from Peys et al. [56]).

and determined that the dissolution of an Fe^{2+}-silicate glass creates a binder phase with both Fe^{2+} and Fe^{3+} oxidation states present. $^{VI}Fe^{2+}$ was found in the tri-octahedral layers (also known as brucite-like layers, present in phyllosilicates like micas), especially in the reaction products of low-calcium slags, while Fe^{3+} was proposed to be located in a more polymerised silicate network.

2.4. Small-angle scattering

Small-Angle X-ray Scattering (SAXS) and Small-Angle Neutron Scattering (SANS) are a pair of techniques that are widely applied to investigate the structure of colloids, porous materials, and polymers; with the advantages of evaluating a wide size range in the nano-size regime (typically 1–100 nm) while allowing for easy sample preparation, as well as providing quantitative information [60]. In the cement chemistry field, SAXS/SANS are mainly used to study microstructural evolution and surface area changes during hydration and drying. The main models used to interpret small angle scattering data are Porod's law [61] and Guinier's approximation [62]. The former gives information on surface and particle interface roughness (S_q) by describing the asymptote of the scattering intensity *I(q)* for large scattering wavenumbers *q*: [60].

$$I_q \sim S_q^{-4} \tag{2}$$

The latter is used to interpret the low-*q* region of the scattering curve giving information on particle size and particle aggregation, and has been used to study the influence of relative humidity on drying shrinkage of cement paste as well as gamma irradiation effects on the nano-porosity of C-S-H by investigating the finer structures [63,64]. The work of Thomas et al. [65] covers the use of SAXS for the determination of the surface area of hydrating cement pastes, while Allen et al. [66] combined SAXS and SANS to provide detailed information about the fundamental water content of cementitious hydrates. In general, the interpretation of small angle scattering measurements is tedious for multicomponent systems, however for single-phase materials, it can provide relevant complementary information.

SAXS is known to be highly sensitive to the presence of heavier atoms, including iron [67,68]. It has been used for the characterisation of iron-rich materials with applications in several fields: in life sciences, it has been used to characterise the structure of iron-bearing biological macromolecules [68]. In biogeochemistry SAXS has successfully been used to characterise iron-organic colloidal nano-aggregates [69]; and in materials science to study the structure and behaviour of magnetic (γ-Fe_2O_3) nanoparticles as they self-assemble when dispersed in ferrofluids [70], as well as liquid crystals such as goethite (α-FeOOH) [71]. In terms of using SAXS for iron-containing cementitious materials, Kriechbaum et al. [72] were able to unravel the fractal geometry of cement pastes microstructure using SAXS. For these experiments, the high-*q* and low-*q* end regions of the SAXS intensities were set to zero to account for additional background effects, mainly due to the fluorescence caused by the presence of iron.

3. Resonance spectroscopy techniques

3.1. Mössbauer spectroscopy

Mössbauer spectroscopy relies on the recoilless absorption and emission of gamma rays (the Mössbauer effect), which only occurs in certain isotopes (Fig. 4a). The most abundant and most studied isotope exhibiting the Mössbauer effect is ^{57}Fe [73,74]. This effect is observed at an energy of around 14.41 keV which is the excitation energy of the core

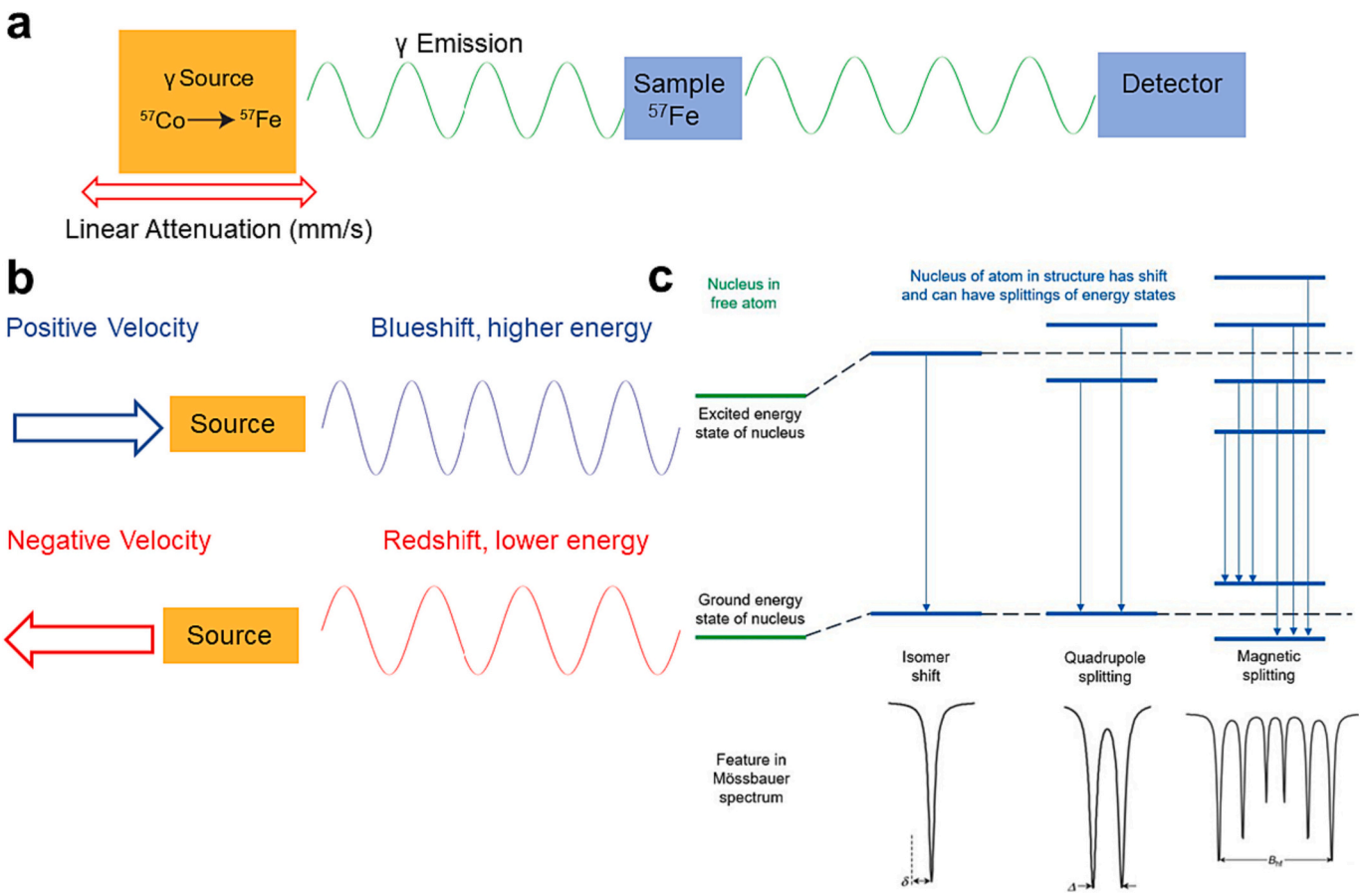

Fig. 4. Mössbauer spectroscopy and its principles. The schematic of the instrument setup and the Doppler effect on γ energy are shown in (a and b). The mechanism behind isomer shift and quadrupole splitting and associated Mössbauer spectra are shown in (c).

electron. This energy slightly varies under the influence of different electron densities, hence bringing the ability to study the speciation of iron using ^{57}Fe Mössbauer spectroscopy [73,74]. The oxidation state, coordination number, neighbouring atoms and crystallinity, have direct influences on the Mössbauer spectrum of ^{57}Fe, enabling a detailed analysis of the state of iron in samples [75,76]. Generally, Mössbauer spectroscopy involves measuring the transmission of the gamma rays of slightly different energies generated through the Doppler effect by moving the gamma source at a certain velocity, and Mössbauer spectra involve plotting the transmission or absorption of the gamma rays with respect to the linear attenuation velocity [73,74] (Fig. 4b). Powder or paste samples are most suited to measurement using Mössbauer spectroscopy. The preparation of powder samples does not require additional processes, apart from the general rules of fineness and avoiding phase transformations during preparations mentioned in the previous sections. The duration of a Mössbauer measurement is about 24–48 h depending on the content of iron and desired signal-to-noise ratio. Paste samples with potential reactions in the solution can be frozen before the measurement [22,77,78], which is usually carried out by dipping the sample holder in liquid nitrogen [79,80]. The measurements themselves are then required to be carried out at 77 K for paste samples [22]. The measurement temperature for powder samples can be varied, and there may be interest in measuring a sample at several temperatures. Shifts in temperature can result in some species being distinguished more easily, or magnetic ordering temperatures can be detected. From a practical point of view, powder samples are mostly measured at room temperature (20 °C) or liquid nitrogen temperature (77 K).

The analysis of the Mössbauer spectra requires specialised fitting software which carries out least-squares minimisation of physically relevant hyperfine parameters (for instance IMSG [81]). This enables fitting of the spectra with realistic contributions of several iron species to extract their hyperfine parameters: isomer shift, quadrupole splitting, magnetic (i.e. hyperfine) splitting, and statistical spread of the quadrupole splitting (or the width of the peaks) (Fig. 4c). The isomer shift is a shift of the central energy of the contribution and relates to the electron density at the nucleus. In the case of iron, the isomer shift increases with decreasing electron density at the nucleus and is always reported with respect to a metallic iron foil reference sample. The isomer shift is especially relevant for iron-bearing minerals as it distinguishes well between Fe^{2+} and Fe^{3+} [82]. Fe^{2+} has an additional electron in the d shell, which does not have a probability of being at the nucleus. It merely shields the nucleus more extensively, causing other electrons to be repelled more from the nucleus, including those with a non-zero probability of being at the nucleus (such as s electrons). Fe^{2+}, therefore, has an increased isomer shift with respect to Fe^{3+} [73,74].

Care has to be taken if different temperatures were used for the measurements. For example, if reporting is carried out with respect to an iron foil at room temperature and measurements have been carried out at 77 K, 0.1 mm/s needs to be added to the isomer shift [73,74].

Quadrupole splitting originates from asymmetry in the electron cloud around the nucleus. This causes the contribution in the spectrum to split into a doublet, and the splitting is quantified by the distance between the two peaks of the doublet. The asymmetry can be caused by the asymmetric filling of spin states, or by an asymmetric environment in terms of neighbouring species. The asymmetry in the filling of spin states provides an additional way to distinguish between different oxidation states. Iron-bearing minerals mostly contain high-spin iron, for which Fe^{2+} has a more asymmetric filling of spin states and much larger quadrupole splitting than Fe^{3+} (Fig. 4c). The effect of the asymmetry in neighbouring atoms on the quadrupole splitting provides an

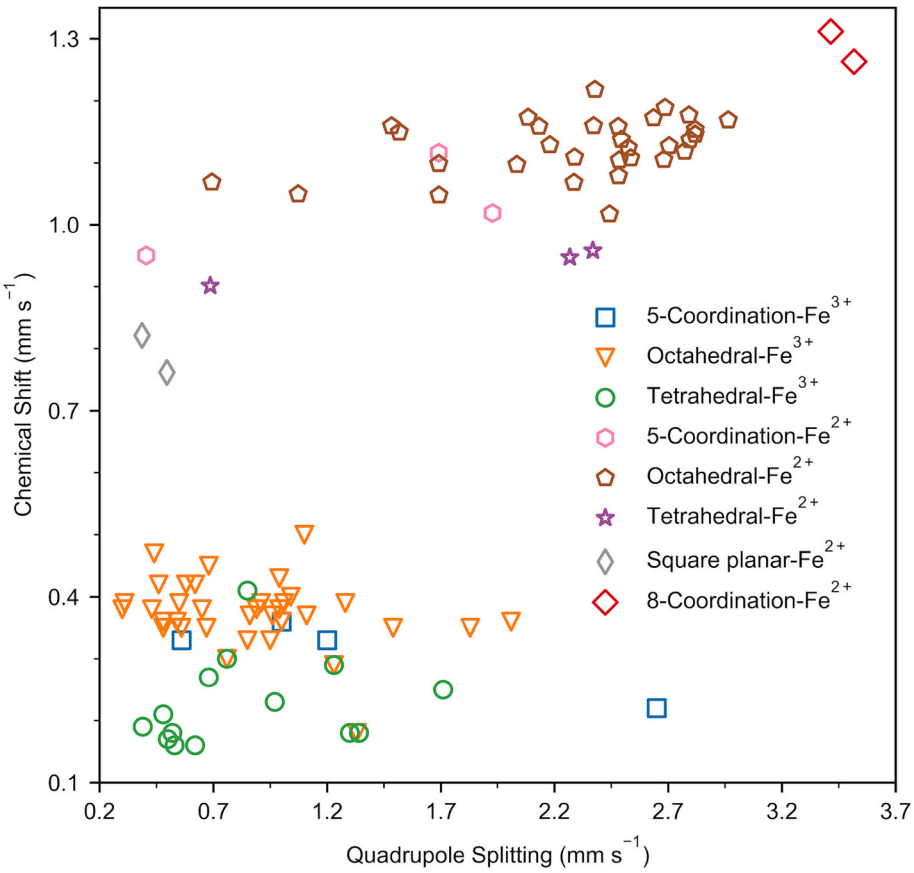

Fig. 5. Isomer (chemical) shift and quadrupole splitting of Fe in several silicate and oxide minerals. Data from Burns and Solberg [76,83].

additional dimension to the analysis of the speciation of iron. More specifically, the asymmetry of the electron cloud is determined by the differences in electronegativity of the neighbouring atoms, as well as their arrangement. The isomer shift and quadrupole splitting are often analysed together to identify the local environment of Fe and the potential phase in which it is present. To this end, these parameters are often plotted as in Fig. 5, which uses data from Burns [83]. An additional hyperfine parameter has to be taken into account when para- or ferromagnetic phases are present. Magnetic splitting leads to a sextet contribution in the spectrum. The final parameter to take into account is the width of the contributions, representing the ordering of the contributing phases. More ordered (crystalline) phases will show iron species with small widths, while iron present in an amorphous phase will show a large peak width.

The ferrite phase in cement is mostly reported as a purely Fe^{3+} phase with a potential range of isomer shifts 0.04–0.65 mm/s (most probable range 0.12–0.50 mm/s) and quadrupole splitting 1.27–1.82 mm/s (most probable 1.50–1.80 mm/s) [84–86]. Magnetic splitting is observed if the ferrite phase has a Fe/Al ratio >1 [87,88]. Due to the significant difference between anhydrous Fe-containing phases such as ferrite and their reaction products (hydrogarnet in pure ferrite-water systems, or in general for iron-containing hydrate phases), Mössbauer spectroscopy can be applied to measure the reaction extent and reaction pathways of the ferrite phase or other Fe-containing constituents [19,87,89]. It is important to note that the absorption areas obtained from Mössbauer spectroscopy are directly related to the percentage of Fe distributed over the different species and do not directly provide the quantity of a certain phase. Recently, the maximum amount of iron uptake by calcium hexaluminate was evaluated using Mössbauer spectrometry for determining the region in the CaO-Al_2O_3- Fe_2O_3 phase diagram that can exhibit magnetic behaviour [90].

Measurements on a Mössbauer spectrometer have a long duration, from 24 h up to a few days, depending on the desired resolution and signal-to-noise ratio. Despite this duration, Mössbauer spectroscopy is suitable for kinetic studies, as measurements can be carried out at frozen nitrogen temperature, decreasing reaction kinetics of cement pastes to near-zero. Mössbauer spectroscopy measurements on frozen solutions have since long been carried out [79,80] and its use for studying kinetics in other fields has been explored [77]. For cementitious materials, measurements of frozen pastes have only recently been carried out to study the kinetics and intermediate reaction products of alkali-activated Fe-rich slag [22,24], but the opportunities are not limited to AAMs or Fe-rich slag, although earlier work was only able to reveal the hydration reactions at a later age due to the choice of measuring at room temperature [87,91]. Alternatively, the traditional hydration stoppage procedures as used for XRD or TGA could be implemented before carrying out Mössbauer spectroscopy, although the effect of these methods on the aluminate hydrates (which might incorporate iron) makes hydration stoppage risky. Furthermore, when studying alternative binder systems such as AAMs, no generally accepted methodology for hydration stoppage exists, making measurements at liquid nitrogen temperature the preferred option at present.

3.2. *Magnetic resonance spectroscopy*

Analysis using magnetic resonance spectroscopic techniques has become increasingly common, especially in the last twenty years, for characterising cementitious materials. These methods can provide detailed information on the local structure of both disordered and crystalline phases present within cementitious matrices.

3.2.1. Nuclear magnetic resonance

Nuclear magnetic resonance (NMR) is a particularly powerful technique for assessing the local coordination environment of specific (non-zero spin) nuclei [92,93]. There are two major uses of NMR in the field of cementitious materials: NMR spectroscopy is used to obtain information regarding the atomic structure and chemical environment around a particular element, whereas NMR relaxometry provides information regarding the bulk structure of the material. Specifically, ^{1}H NMR relaxometry has been used extensively to evaluate the microstructure and porosity of cementitious materials at different scales [94–96].

However, the presence of Fe-containing species leads to issues with the shifting and broadening of NMR spectra [92]. This arises from the paramagnetic nature of Fe, with unpaired electrons causing significant shielding of the measured nuclei from the externally applied magnetic field (B_0) and distortion of measurements [93]. Thus, cementitious materials containing significant amounts of Fe^{3+}, such as grey Portland cement, ferrite-rich sulfoaluminate cements, or fly ash-based binders, may not be suitable for NMR analyses [92]. In some cases, washing with oxalic acid or hydrochloric acid, or magnetic separation of paramagnetic particles, has been used to improve the quality of NMR spectra [97–99]. One of the common ways to reduce the peak width of NMR is to use a higher magnetic field, and based on a study on kaolinite samples, the benefit of using a higher magnetic field increases with paramagnetic Fe content [99]. ^{27}Al NMR studies conducted on single-phase C_4AF have shown that increasing Fe content dampens and broadens the acquired signal through shielding effects; nevertheless, Al^{IV} and Al^{VI} signal contributions may still be resolvable [92,100,101]. ^{29}Si NMR measurements of Portland cement is also affected by the proximity of Fe^{3+} ions, either from intermixed C_4AF or as incorporated guest ions in C_3S or C_2S [92,102–104]. The presence of paramagnetic Fe species reduces the spin relaxation time, which enables using a lower relaxation delay time, which enables quicker ^{29}Si NMR data collection, although quantitative information regarding different types of silicates present are hard to obtain because of peak-broadening because of presence of iron [105].

The presence of Fe-containing species also alters the spin relaxation times, and in turn, affects the microstructure and porosity measurements. For ^{1}H NMR relaxometry, both spin-spin (T_1) and spin-lattice (T_2) surface relaxation times decrease linearly with paramagnetic impurities such as Fe_2O_3, as described theoretically [106], and verified experimentally on iron (III)-doped kaolin clay and cement stone samples [96,107]. This affects both T_2-relaxometry, generally used to measure pore sizes, as well as T_1-T_2 correlation relaxometry, which can be used to determine the amount of water moving from different pore sizes [108–110] for C-S-H and cement paste samples. Carroll et al. [111] correlated the changes in T_2-relaxation time with changes in magnetic susceptibility and used the corrected T_2-relaxation time to measure water content in Fe-rich rock samples. Zhou et al. [112] used low field ^{1}H NMR relaxometry to study the effect of soluble paramagnetic Fe (III) on the polymerization process of alkali-activated metakaolin. This offered the advantage of a lower paramagnetic effect compared to high-field NMR.

3.2.2. Electron paramagnetic resonance

While issues arise with measuring Fe^{3+}-rich compounds with NMR, electron paramagnetic resonance (EPR) spectroscopy can be used as an alternative. EPR works from a similar principle to NMR, but electron spins are probed rather than the nuclear spin. This means that EPR can only be used to measure atoms with unpaired electrons and, unlike NMR where the magnetic field is held constant, in EPR the magnetic field strength is varied, and the radiofrequency is held constant.

EPR is a widely available analytical technique but is not commonly used in the characterisation of cements. However, studies have been undertaken on anhydrous cement components and hydrated assemblages. EPR studies have tracked the chemical environment of Fe through the progress of hydration reactions and setting of PC and PC/metakaolin blends [113], and differentiated between Fe(III) as iron oxide or as high-spin, low crystal field symmetry phases (i.e. clinker and hydrate phases) [114–116]. EPR was also used in understanding the effect of Fe^{3+} ions on the precipitation of C-S-H at different pH levels [117]. Fe^{3+} was found to be distributed uniformly when C-S-H precipitated at a low pH (<11) in the absence of ferrihydrite, whereas at a high pH level, ferrihydrite formed and restricted iron incorporation in C-S-H. In laterite-based cements activated using phosphoric acid, the formation of Fe-phosphate binder phases (such as $FePO_4$) has also been inferred using EPR [118].

4. X-ray absorption spectroscopy

X-ray absorption spectroscopy (XAS) can be used to provide information about the oxidation state and local coordination environment of a given element [119,120]. This technique works on the principle of probing a given atom over the energy range required for electronic excitation of a given atomic orbital, in order to induce constructive and destructive interference with neighbouring atoms and thus infer details of the local structure. In the case of Fe, the K atomic-edge is often probed, and the energy required for electronic excitation (7.112 keV) means that either laboratory-based or synchrotron techniques can be used [121,122], though laboratory-based X-ray absorption techniques have not yet been reported in the field of cementitious materials. X-ray absorption near edge structure (XANES) refers to the region of features at or near the absorption edge, extending to ~50 eV beyond the edge, while extended X-ray absorption fine structure (EXAFS) refers to the region of oscillations extending beyond the edge and XANES region [29].

A suite of known standard compounds with a range of oxidation states will often also be measured to compare to sample data. For probing Fe in cements, this could include iron metal, iron oxides/(oxy) hydroxides, and/or pure-phase Fe-containing hydrate phases. In particular, least-squares linear combination fitting can be a useful technique for determining the percentage contribution of a spectral signal that is comparable to that of known Fe-containing standards with well-characterised structures. Examples of the XAS spectra obtained for Fe in its three most commonly encountered oxidation states (0, +2 and +3) are given in Fig. 6.

4.1. Sample preparation

The preparation of samples for X-ray absorption spectroscopy measurements can be dependent on many factors. One of the most important considerations is ensuring that the concentration of Fe within the sample is sufficient to obtain a signal. If the exact chemical formula of the material is known, the amount of sample required to obtain a sufficient signal for transmission measurements can be determined using a transmission calculator (e.g. Hephaestus [124] or others). However, considering cementitious materials, the exact composition can be difficult to determine, especially where Fe may be present at low levels. In this case, increasing the amount of sample to obtain fluorescence measurements may be favoured, whereby corrections may be applied to account for self-absorption [119].

For measurements of bulk XAS whereby an average signal of Fe is resolved from the whole sample, powdered forms of the material can be prepared into mechanically stable pellets using a binding agent (e.g., polyethylene glycol (PEG)). In the case of spatially resolved studies (μ-XAS), sample surfaces or thin sections may be measured where the material is heterogeneous and Fe distribution is not uniform, as is often the case for cement monoliths.

4.2. X-ray absorption near-edge structure (XANES)

XANES is sensitive to the oxidation/valence state of the atom, as well as the geometrical arrangement (bond angles) of neighbouring atoms. At

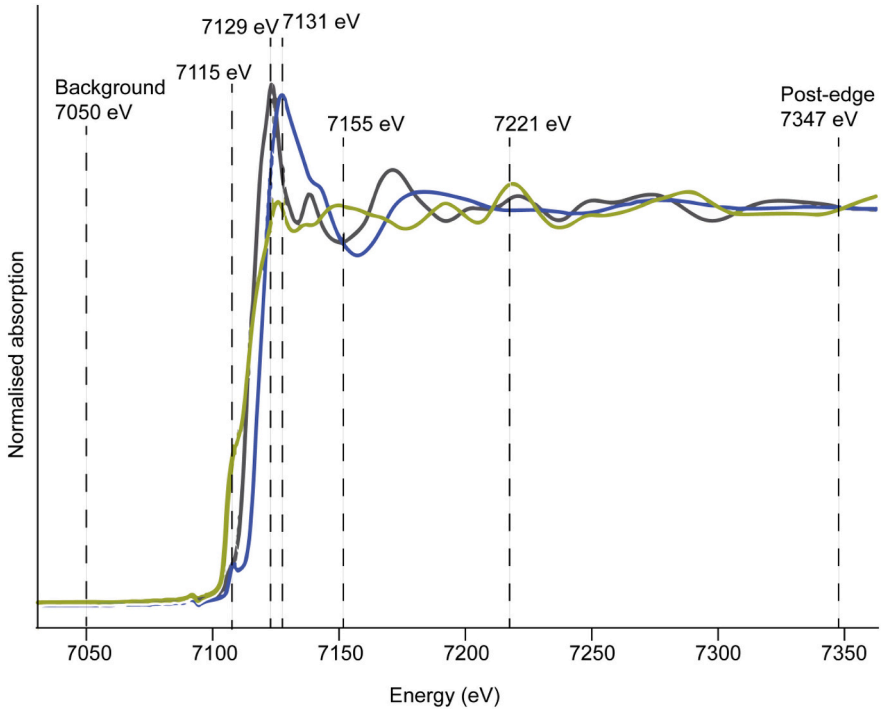

Fig. 6. Experimental XAS spectra of Fe(0) (green line), Fe(II) (black line) and Fe(III) (blue line) reference compounds, from [123]. (For interpretation of the references to colour in this figure legend, the reader is referred to the web version of this article.)

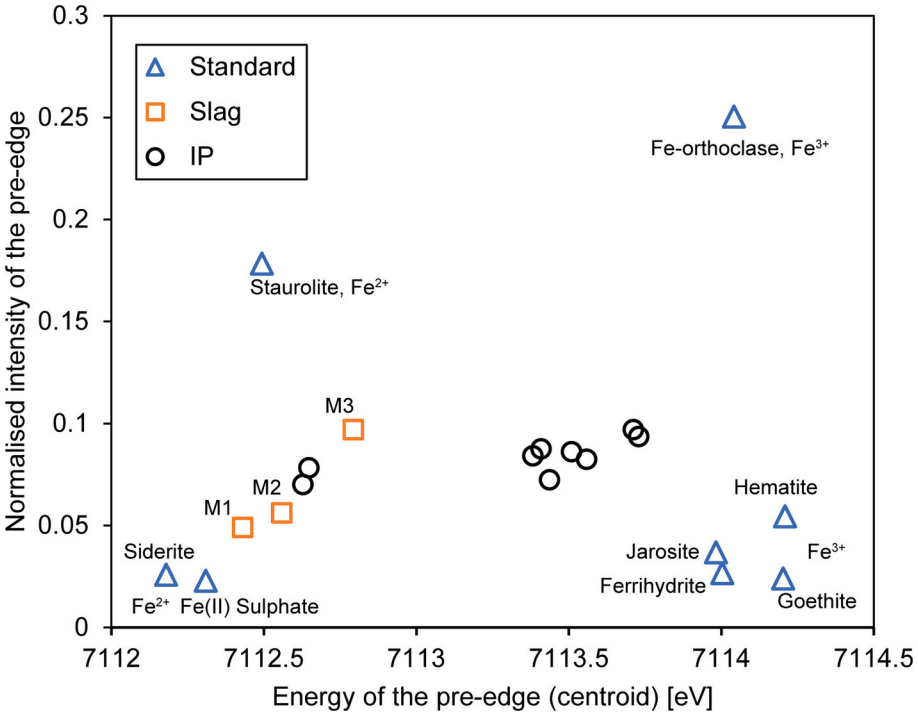

Fig. 7. Plot of normalised integrated area intensity vs position (peak centroid) of the pre-edge features of model compounds (standards), slags (M), and inorganic polymers (IPs), from [26]; adapted from [126,127].

the K-edge, Fe displays pre-edge features that are a result of 1s → 3d bound state electronic transitions [125]. The position (i.e., energy) of this pre-edge peak shows a good correlation with the oxidation state and coordination number of Fe. Fig. 7 displays a plot of the energy assignment of the central positions of these pre-edge transitions for some standard iron compounds [26]. The size and intensity of these pre-edge features can be used as a fingerprint for further identification of the Fe coordination environment.

4.3. *Extended X-ray absorption fine structure (EXAFS)*

EXAFS analysis can yield information about interatomic distances

and coordination numbers of neighbouring atoms. However, the distances measured in EXAFS are electron cloud-electron cloud probability densities and will therefore deviate from the nucleus-nucleus distances obtained in PDF analysis with an order of magnitude of 0.6 Å (shorter distances for EXAFS). Furthermore, while PDF analysis considers all atoms in a certain material, EXAFS provides a selective view of the neighbours of the atom of which the absorption edge is measured. Similar to PDF analysis, however, prior knowledge and reasonable assumption(s) are required to assign features to particular neighbouring atoms. Table 3 shows some assignments for the fits of iron minerals and iron environments in cements. EXAFS fitting models can be used to determine the coordination numbers and interatomic distances of nearest (usually oxygen) and next-nearest neighbours of Fe [15,119], however, this can often be difficult in multi-phase systems where there are multiple contributions from the presence of different phases.

4.4. Fe K-edge X-ray absorption spectroscopy applied to cementitious systems

In a recent study by Mancini et al. [79], the speciation of iron in BFS cements was investigated using the Fe K-edge XANES region; bulk XANES measurements of various slag-containing cement and concrete samples were compared to the spectra of known Fe compounds. Linear combination fitting was applied to determine the percentage similarity of the sample signals to that of the standards. For example, the majority of the signal for a lab-produced super-sulfated slag cement composite was attributable to Fe(0) (i.e., Fe metal particles entrained in the BFS), with the remainder being attributed to Fe(II)S and Fe(III) in Fe_3O_4. This indicates the applicability of XANES to identify the oxidation state and local geometry of Fe within a cementitious matrix. However, when applied to an unhydrated slag-containing cement, the linear combination fit yielded a high residual (R-factor), and the XANES signal was attributed to only two different Fe species, i.e., the Fe-rich clinker phase C_4AF (~54 %) and Fe(0) (46 %) from the slag. This was suggesting that a Fe-containing species was missing from the fit (potentially a glassy Fe fraction from the slag); linear combination fitting methods are therefore only fully effective when all possible phases present are included in the fit.

Further to this, Dilnesa et al [86] measured bulk XANES and EXAFS signals to discriminate the formation of Fe-substituted hydrate phases from purely Al-containing hydrate phases in hydrated Portland cements, by comparison to Fe-containing reference compounds. Linear combination fitting was applied to the EXAFS spectra to determine the independent components contributing to the signal. The contributions of the Fe-phases were shown to evolve over time; the unhydrated clinkers displayed a signal that was only attributable to ferrite, but with increasing ferrihydrite (~4–16 h) and hydrogarnet (>~16 h) predominance as hydration proceeded. EXAFS model fitting was not attempted, presumably due to a combination of Fe coordination environments being present (i.e., making single-phase fitting difficult).

Vehmas et al. [129] also used both bulk XANES and EXAFS to determine differences and similarities in the Fe chemical coordination environments of a mortar and concrete made using a silica fume/slag Portland cement blend. The Fe environment in the mortar was likened to a combination of C_4AF, C_2F or Fe(III) substituted C-S-H; this was similar for the concrete, but with additional features in the XANES and EXAFS regions, probably arising from some amount of Fe in the granitic-based aggregate used. EXAFS model fitting was again not performed in this case, rather the XANES and EXAFS signals were used as a qualitative comparison.

In a study by Rose et al. [15], EXAFS model fitting was performed to determine the atomic environment of Fe after C_4AF hydration (see Table 3). The fit indicated that the Fe environment was dominated by an amorphous FeOOH phase, with a small Fe—Ca contribution from what was inferred to be Fe-substituted hydrogarnet [15].

The attentive reader would have noticed that different authors have delivered different hydrate phase assemblages as a result of C_4AF hydration based on XANES and EXAFS studies. The interpretation of the results can be ambiguous and complementary characterisation is recommended.

As well as the bulk XANES measurements discussed previously, Mancini et al. [123] also mapped the surface of hydrated slag cement thin sections exposed to different environmental conditions using μ-XRF and μ-XANES. Redox maps, obtained from μ-XANES based on energy discrimination, were produced to determine the oxidation state of Fe regions. Sea water exposure oxidised all the Fe(0) species present in the slag cement, while river water did not as presence of Fe(0) was observed in the hydrated slag cement sample exposed to river water.

5. X-ray fluorescence spectroscopy

In addition to X-ray absorption, X-ray fluorescence (XRF) can be used to obtain spectral signals at atomic edges. Fluorescence measurements differ from transmission measurements in that fluorescent X-rays or Auger electrons (that accompany the dropping down of core-hole filling electrons) are measured [76]; the sample usually has to be oriented at 45° relative to both the incident beam and detector in order to measure these. XRF is a very common technique used in both industry and academia to evaluate the elemental and oxide composition of cementitious materials. XRF mapping can be useful for obtaining spatially resolved elemental maps of cement or other mineral surfaces. Micro-XRF mapping has been used before for mapping chlorine ingress, as well as

Table 3
EXAFS model fitting assignments of some iron minerals and iron environments in cements.

Environment/phase	Neighbour(s)	Distance/Å	Coordination numbers	Comments	Reference
Goethite	O	1.90 ± 0.02	3.0 ± 0.8	Single phase goethite standard	Ma et al. [128]
	O	2.04 ± 0.02	3.0 ± 0.8		
	Fe	3.00 ± 0.03	2.0 ± 0.8		
	Fe	3.22 ± 0.07	1.9 ± 1.2		
	Fe	3.39 ± 0.02	3.9 ± 0.9		
Hematite	O	1.94 ± 0.03	3.0 ± 0.9	Single-phase hematite standard	Ma et al. [128]
	O	2.10 ± 0.02	3.0 ± 0.8		
	Fe	2.92 ± 0.07	1.4 ± 0.9		
	Fe	2.97 ± 0.03	3.0 ± 0.9		
	Fe	3.37 ± 0.01	2.6 ± 0.6		
Hydrated C_4AF	Fe	~3	2–3	Edge sharing between Fe octahedra in Fe hydroxide or oxyhydroxides.	Rose et al. [15]
				Double corner linkages in Fe hydroxide or oxyhydroxides	
	Fe	3.45	~0.2	Fe-substituted hydrogarnet	
		~3.6			
	Ca		~2		

irradiation damage in concrete [130,131].

Although XRF provides only elemental mapping, it is possible to detect and quantify presence of different minerals by combining the maps of different elements. Pyrites were identified and quantified in aggregate samples before using micro-XRF mapping [132]. One of the drawbacks of micro-XRF compared to other common elemental mapping technique such as scanning electron microscopy coupled with energy dispersive spectroscopy (SEM-EDX) is its higher spot size. However, specialised synchrotron-based instruments can overcome this difficulty and provide nanoscale information. For example, Bernal et al. [18] carried out nanoprobe XRF mapping on the surface of alkali-activated slag binders, at a photon energy of 10.5 keV, allowing the detection of elements with $Z \geq 13$. It was observed in the maps that Fe-rich particles from the slag precursor remained intact after activation, showing no detectable incorporation into the binder phases. The same instrument was used by Provis et al. [133] to analyse elemental distributions in alkali-activated fly ash specimens; by correlating chromium and iron distributions, they demonstrated that the chromium present in the fly ash (at a bulk concentration below 0.02 %) remained tightly correlated with the undissolved ferrite spinel phases after alkali-activation, leading to the conclusion that this potentially hazardous element was not in fact being solubilised or released through the alkali-activation process.

6. Vibrational spectroscopy techniques

6.1. Infrared (IR) spectroscopy

Infrared (IR) spectroscopy allows the identification of particular bond configurations by measuring the observed signal when IR light interacts with matter [134]. Fe—O bonds can be directly probed (examples given in Table 4), or the effect of the presence of Fe on the interaction of other bonds can be evaluated. It has been observed that Fe^{3+} substituted into Al^{3+} sites results in a broadening and dampening of the observed IR signals for Al—O bonds, specifically observed in ye'elimite (tetrahedral) [13], C_3A (tetrahedral) [135], and AFm phases (octahedral) [136,137].

Furthermore, Liang & Nanru noted that IR signals for SO_4^{2-} (from S—O bonds) increased in intensity in the presence of Fe^{3+} (substituted for Al^{3+}) in AFm phases, as a result of the higher electronegativity of Fe than Al [136]. However, this was not corroborated by Ndzila et al. in Fe^{3+}-substituted ye'elimite [13].

The most widely probed information from IR spectroscopy in cementitious systems is the structure of glassy or nano-crystalline silicates. In conventional cements and most Fe-rich alternatives, the Si—O bands are the most prominent features visible in the IR spectra. This means that (1) the bands of Fe—O bonds can be confused with the Si—O rocking vibrations (400–600 cm^{-1}) or Si—O stretching bands (800–1100 cm^{-1}) and that (2) the influence of iron on the configuration of the silicate phases can be revealed or confirmed. Mostafa et al., for instance, used IR to demonstrate increased polymerisation and cross-linking in Fe^{3+}-substituted C-S-H, as a result of decreases and increases in Q^1 and Q^3 Si—O signals, respectively [141]. The synthesis of alkali-activated fayalitic slag was monitored ex situ by Peys et al. to reveal the kinetics of the formation of the silicate network by the shifts in the Si—O stretching band [22]. However, in general, the interpretation of the broad Si—O bands can usually provide a multitude of potential explanations. Therefore, the use of IR spectroscopy can best be used for confirmation of knowledge obtained from other measurements or for monitoring changes of which the nature is known, rather than for trying to uncover details of unknown structures.

6.2. Raman spectroscopy

Raman spectroscopy is complementary to IR spectroscopy, as both concern interaction between photons and molecular chemical bonds. However, Raman-active interactions involve a change of polarisability through inelastic scattering, whereas IR-active interactions involve a change of dipole moment through absorption [142] . Raman spectroscopy generally involves exposing the sample to a monochromatic high-intensity laser light source and measuring the wavelengths and intensities of the scattered light. As inelastic scattering of light is a low-probability phenomenon and has a low intensity, it is difficult to distinguish the Raman peaks from fluorescence for iron-rich materials, including PC clinker. Even though it is generally accepted that a high amount of iron causes a high background, Richardson et al. [143] argued that the background signal further increases with grinding because of increased interparticle scattering as well as organic grinding aids present in Portland cement clinker. Washing OPC clinker with organic solvents, photobleaching to reduce fluorescence, and finally immersing the sample in low-fluorescence, high-refractive index immersion oil for reducing inter-particle scattering was found to be effective in obtaining low-background Raman spectra.

In general, high-wavelength laser sources have been used to identify the presence of commonly encountered Fe oxides and oxyhydroxides, among other Fe minerals (see Table 5). The Raman spectral profile changes with laser wavelength because of changes in fluorescence, Raman intensity, and particle scattering, but the peak locations or Raman shifts are not dependent on the source laser wavelength.

Fig. 8 shows the Raman spectra of different Fe-bearing minerals commonly present in cementitious materials. When using Raman spectroscopy to identify different iron-bearing hydroxides and oxides, it is recommended to start the measurement using a very low-power laser source (0.01 mW) and then slowly increase the laser power (>1 mW) to obtain a stronger signal, as higher laser power can increase the temperature of the sample and transform iron-containing minerals (e.g. ferrihydrite, magnetite, lepidocrocite) to hematite [144].

As with IR, the substitution of Fe^{3+} into Al^{3+} sites can also be indicated by intensity changes in the Raman signal. In one of the earliest studies using Raman spectroscopy on cementitious materials, Conjeaud and Boyer [145] noted that synthetic calcium alumino-ferrites have a broad peak at around 750 cm^{-1}, and the peak is shifted towards a lower Raman shift with an increase in Fe/Al ratios. Dariz et al. noted that Raman band positions could be used to determine the stoichiometry of $C_2A_xF_{1-x}$ phases [146]. Further to this, Gómez-Nubla et al. also observed

Table 4
Example IR assignments to some Fe—O bonds in cementitious environments/minerals.

Wavenumber(s)/cm^{-1}	Assignment	Environment	Reference
595	Fe-O, as tetrahedral [FeO_4]	C_4AF in Fe-rich CSA cements	[138]
661, 960	Fe-O, as octahedral [FeO_6]	Fe-containing AFm (carbonate) phases	[137]
630, 670 (weak)	Fe-O ("Fe^{3+}") as tetrahedral [FeO_4]	Fe (and Zn)-substituted alinite cement	[139]
500–600, 280–360	Mixed vibrational modes of octahedral [AlO_6] and [FeO_6]	Fe-containing AFm phases	[136]
	Fe-O, as octahedral [FeO_6]		
472			
660	Fe-OH, as octahedral [FeO_6]	Fe^{2+}-containing phyllosilicate	[140]

Table 5
Example Raman assignments for some Fe minerals in cementitious environments (intensities of bands are not reported here). Major narrow and high intensity peaks are underlined when three or more peaks are reported in the literature.

Phase name	Chemical formula	Wavenumber(s)/cm^{-1}	Environment	Reference	Excitation wavelength (nm)
Goethite	α-FeO(OH)	204, 245, 298, 385, 479, 549	Diagenetic ferruginous cements (DFC) derived from slag and iron-rich wastes	[150]	785
		248, 300, 384, 475, 529	Black slag	[147]	785
		700, 1410	Passivating oxyhydroxide film on rebar immersed in cement-saturated solution (mixed with lepidocrocite)	[151]	532
Hematite	α-Fe_2O_3	204, 225, 242, 292, 410, 486, 611, 1310	DFC	[150]	785
					785
		223, 288, 408, 497, 608	Black slag	[147]	785
Lepidocrocite	γ-FeO(OH)	216, 249, 306, 343, 374, 525, 646	DFC	[150]	785
					785
		215, 248, 305, 346, 375, 525, 646	Black slag	[147]	785
Magnetite	Fe_3O_4	105, 208, 668	DFC	[150]	785
		314, 477, 558, 680	Black slag	[147]	785
Maghemite	γ-Fe_2O_3	351, 495, 665	DFC	[150]	785
		276	Passivating oxyhydroxide film on rebar immersed in cement-saturated solution (dehydrated)	[151]	532
Limonite/hydrated goethite	FeO(OH)·nH_2O	244, 298, 394, 468, 551, 658, 1360	DFC	[150]	785
		296, 396, 470	Black slag	[147]	785
Wüstite	FeO	657	Slag grain in lime mortar	[152]	532
Siderite	$FeCO_3$	189, 294, 730, 1087	Natural mineral	[153]	780
Magnesioferrite	$MgFe_2O_4$	488, 616	DFC	[150]	785
		327, 435, 613	Black slag	[147]	785
Calcium aluminoferrite (hydrated)	$[(Fe,Al)O_4^{5-}]$	280	Hydrated C_4AF	[154]	785
Calcium aluminoferrite	$[(Fe,Al)O_4^{5-}]$ or $[(Fe,Al)O_6^{9-}]$	256, 308, 737	Synthetic C_4AF	[145]	514
Iron sulfide(s)	S^{2-}	218	C_4AF corroded in the presence of H_2S	[154]	785

displacement of bands for magnetite in black slag, as a result of stoichiometric substitution for Co, Ni and Al or due to slight differences in the Fe oxidation state [147]. Fe-substituted ettringite also showed a change in the Raman peak, moving to a higher wavenumber Raman shift for the major peak that was observed at 990 cm^{-1} for pure ettringite [148].

In terms of C-S-H, Ovcharenko et al. observed an increase in Q^1 sites, a decrease in Q^2 and a loss of Q^3 Raman signals resulting from Fe^{3+} incorporation, which was interpreted as the presence of the Fe^{3+} preventing the formation of extended silicate chains [149]. These Raman spectroscopic results agree with the IR study of Mostafa et al. [141] who showed a decrease and increase in Q^1 and Q^3 Si—O signals, respectively.

7. Microscopy

7.1. Optical microscopy

Optical microscopy (or light microscopy) can provide information on clinker microstructure, including bulk composition, raw feed preparation, burning conditions, and cooling rate [9,156,157]. Most commonly, clinker samples are analysed in the form of polished or etched sections in reflected light. More information can be obtained by the analysis of thin sections in transmitted light under a polarised light microscope (or petrographic microscope). General information on sample preparation for clinker analysis with optical microscopy (non-specific for iron-rich clinkers) can be found in [158]. Etching with HF, HNO_3 or other etchants is commonly used for clinker analysis for phase identification.

Ferrite is resistant to etching and appears brightly reflective when viewed in reflected light [158] (Fig. 9). Ferrite typically shows crystals of dendritic and needle-like habit embedded in a matrix of aluminate and shows pleochroism under transmitted light [9]. The crystal structure of ferrite is influenced by the cooling rate: in slowly cooled clinkers, the aluminate and ferrite phases may be coarse-grained and well-developed prisms of C_4AF can be recognised, with broad forms dominating in clinkers with low Al/Fe ratio, and small needle-like forms dominating in clinkers with high Al/Fe ratio. In rapidly cooled clinkers, the aluminate and ferrite phases may be fine-grained and mixed on a micrometre scale [158] and the most common habits of ferrite are long, narrow prisms or dendritic growths in clinkers with low Al/Fe ratio. The phases of the solid solution $Ca_2(Al_xFe_{2-x})O_5$ are not distinguishable by optical microscopy [158].

Light microscopy can be used for quantitative phase analysis however, the aluminate and ferrite phases are often very difficult to measure separately due to their similarity in chemical composition and crystal system – both being orthorhombic [9,159]. Point counting is a common method used for phase quantification by optical microscopy, but the aluminate and ferrite phases are also difficult to quantify due to their small crystal size [159]. Therefore, aluminate and ferrite are often taken together and referred to as “interstitial phase”.

Reflected light microscopy has been used by Guo et al. [160] to investigate the microstructure of high-Fe clinkers. Samples were prepared by cutting and mounting in epoxy resin, polishing with diamond paste, and final etching in 1 % NH_4Cl. Their results suggest that the presence of iron affects the grain size of alite, which displays a larger size with increasing iron content. Zhao et al. [161] used petrography to characterise iron-rich clinkers produced using steel slag and also found that alite crystals become larger with increasing iron content. Shao et al. [162] used a metallographic microscope to investigate the microstructure of clinkers with a high Fe/Al ratio in the ferrite phase. They also found that the presence of iron affects alite grain size similar to past literature [160,162], however, in this study, higher iron content was linked to a smaller alite grain size, likely due to a higher amount of ferrite interstitial phase which leads to a higher density of alite nuclei at the expense of alite crystal growth.

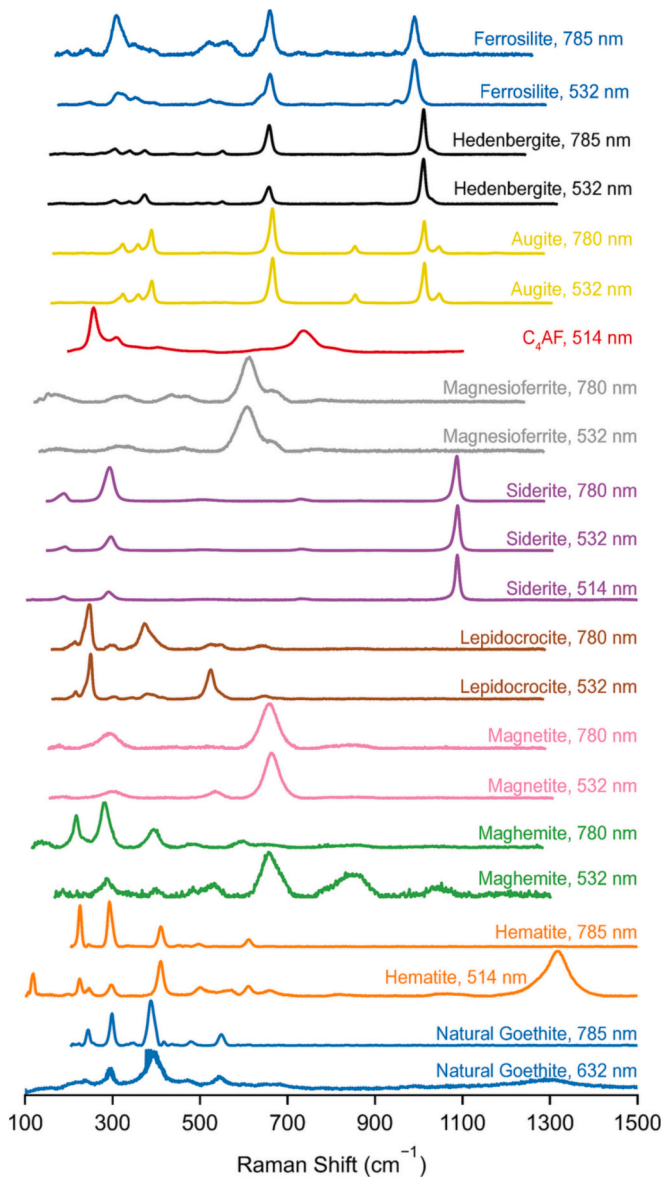

Fig. 8. Raman spectra of different iron-bearing minerals collected using different laser source wavelengths collected from the RRUFF database [153] and literature. Natural Goethite (632 nm [155] and 785 nm (RRUFF id: X050091)), Hematite (514 nm (RRUFF id: R040024) and 785 nm (RRUFF id: X050102)), Maghemite (532 and 780 nm (RRUFF id: R140712)), Magnetite (532 and 780 nm (RRUFF id: R080025)), Lepidocrocite (532 nm and 780 nm (RRUFF id: R050454)), Siderite (514, 532, and 780 nm (RRUFF id: R050262)), Magnesioferrite (532 and 780 nm (RRUFF id: R070127)), Calcium aluminoferrite (514 nm) Augite (532 and 780 nm (RRUFF id: R110063)), Hedenbergite (532 and 785 nm (RRUFF id: R070236)), Ferrosilite (532 and 785 nm (RRUFF id: R070386)). All the data were collected for unoriented samples and background signal was subtracted.

7.2. Electron microscopy

Electron microscopy is a powerful tool that is commonly used to assess cementitious materials. As with all microscopic techniques, appropriate sample preparation is essential for successful data acquisition. Full details on sample preparation methods for a range of cementitious materials can be found in [163].

7.2.1. Scanning electron microscopy

Scanning electron microscopy (SEM) enables surface imaging and mapping of cement surfaces using an accelerated beam of electrons. When combined with energy dispersive spectroscopy (EDS) analysis, the location of Fe, or its incorporation into mineral phases, can be quantified. In order to determine Fe content accurately using its Kα characteristic X-ray emission, an accelerating voltage of around 15 kV is required due to its higher excitation energy (~6.4 keV) [163], whereas Fe detection can be achieved with a much lower accelerating voltage (<10 kV) through using the Lα characteristic X-ray emission with excitation energy 0.7 keV. A lower accelerating voltage should be chosen to improve the spatial resolution of SEM-EDS analysis where quantifying Fe content is not required.

Discrete metallic Fe and Fe oxides, embedded in cement matrices, are easily distinguishable in backscattered electron micrographs as “bright” particles [164,165], resulting from the higher atomic number (Z) of Fe and in turn the higher elastic scattering of incident electrons. The distribution and morphology of the ferrite phase in clinker is often studied by back-scattered electron microscopy (Fig. 10).

In particular, Crumbie et al. used SEM-EDS to determine that both orthorhombic and cubic aluminate phases in laboratory-produced clinker can contain up to 4 wt% Fe_2O_3 compared to industrial clinkers, at the expense of ferrite formation [159]. Dominguez et al. also used EDS to calculate stoichiometric formulas for Fe-substituted apatite phases, formed during cementation of steelwork dusts [166]. EDS mapping of the different elements present in the sample could be utilised to identify the different phases present in the sample as well as their chemical composition [167]. This is a valuable tool for identifying the different phases present in the sample more confidently, which then can be used for quantitative X-ray diffraction analysis as well. Similarly, electron backscatter diffraction (EBSD) can directly reveal the distinct phases and crystal orientation in the microstructure of cements [168]. EBSD data, in combination with EDS, can be used to identify the crystal structure and chemical formula of ferrite present in the cement clinker [168]. EBSD can also measure the crystallite size of the interstitial phases [168], and the detailed crystallographic information obtained from the SEM-EBSD and SEM-EDS data could be useful for understanding cement properties and performances.

7.2.2. Transmission electron microscopy

Transmission electron microscopy (TEM) can be useful for observing minor phases within clinkers or cements, which may be Fe-containing. Richardson et al. characterised the interstitial phase of an oil-well cement clinker (with a characteristically high Fe:Al ratio) and determined it to be predominantly ferrite, with a Fe:Al ratio of ~2 [170]. Further to this, inner product C-S-H assemblages arising from the hydration of Portland cement or slag blends have been shown to be intermixed with Fe-rich hydrogarnet precursors or Fe-substituted AFm and brucite phases, respectively, through observation by TEM [171,172]. The use of EDS coupled with TEM enables the measurement of concentrations of Fe in the cementitious materials. Astoveza et al. [140] studied the fate of the iron where iron-rich slag from a lead-zinc plant was hydrated with a ternary blend of calcium aluminate cement, Portland cement, and calcium sulfate using TEM-EDS. The authors found no evidence of Fe present in ettringite, strätlingite or other AFm phases, but instead, Fe was detected in the amorphous hydrated gels – aluminium rich gels when no Portland cement is used, and calcium aluminate silicate gels for Portland cement containing formulations.

Similar to coupling of EDS with TEM, coupling Electron Energy Loss Spectroscopy (EELS) with TEM provides opportunity to quantify iron with different oxidation states at a very high resolution. Marris et al. [173] were able to quantify the change of iron speciation in the fine-particle emissions from a Fe—Mn alloy plant from the chimneys to the near-field air samples. Quantification of the Fe(II) and Fe(III) species in Fe-rich 1:1 phyllosilicates resulting from interactions between metallic iron and smectite clays were also performed using this technique [174]. TEM-EELS has also been used to investigate effects of minor elements (Si and Ti) in ferrites. Gloter et al. [175] found that the iron oxidation state

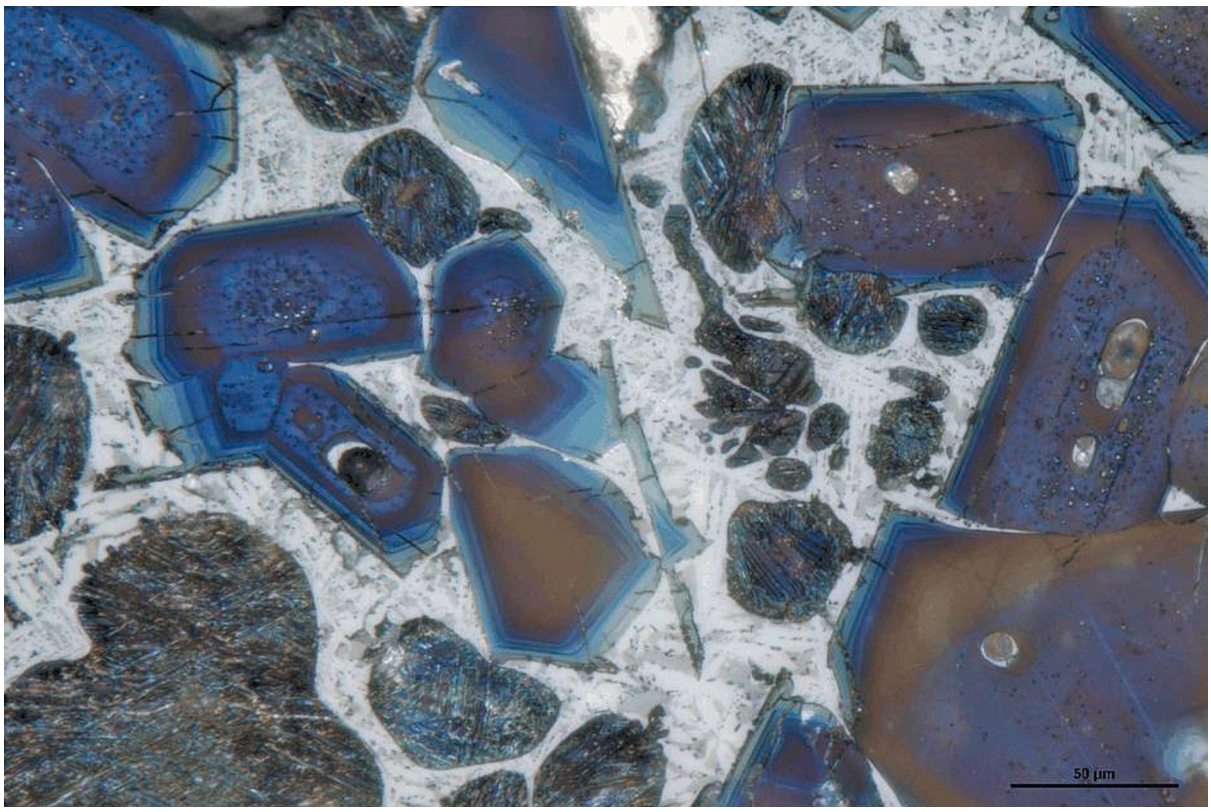

Fig. 9. Optical micrograph of a nital-etched specimen of Portland clinker (nital is a solution of nitric acid and alcohol). Alite grains are blue-brownish and generally angular showing growth zones, while belite grains are rounded and have a fine lamellar appearance. The light-coloured interstitial phase represents an intergrowth of C_3A (darker zones) and ferrite (white elongated crystals) (photo by P. Stutzman – reproduced with permission). (For interpretation of the references to colour in this figure legend, the reader is referred to the web version of this article.)

did not reduce significantly when tetravalent cations (Si^{4+} and Ti^{4+}) were incorporated into the brownmillerite structure, implying that charge compensation occurs through incorporation of extra oxygen atoms. A TEM-EELS study on calcium aluminate clinker found both brownmillerite and perovskite type structures present in ferrite, with perovskites being highly oxygen-deficient which allows incorporation of silicon [176].

8. Thermal analysis

Thermal analyses are routinely used in cementitious materials especially to quantify free and bound water content, different hydration phases (e.g., portlandite, ettringite, monosulfate), carbonates (e.g., calcium carbonate, monocarbonate, hydrotalcite-group phases), unburnt carbon content, and sulfates (gypsum, hemihydrate) mainly through thermogravimetric analysis (TGA), which measures mass loss (or gain) while heating the sample under a controlled environment [23]. Sometimes another characterisation tool such as a mass-spectrometer or FTIR is coupled with TGA to measure the chemical compositions of the gas. TGA can be performed in different purging gases, generally argon, nitrogen, air, or oxygen gases are used to provide either inert or oxidising environments. Another commonly used thermal analysis tool is differential scanning calorimetry (DSC), which can identify the phase transitions and measure the enthalpy of transition. DSC has been used to quantify the gypsum and hemihydrate content in cements [177], freeze-thaw response of concrete [178–180], hydration kinetics [181–184], and reaction stoichiometry [185].

Many Fe-bearing minerals and oxides are known to generally oxidise and undergo phase changes at high temperatures, which can affect the TGA or DSC measurements (Table 6). Oxidation of Fe^{2+}-bearing minerals can increase the mass of the sample in TGA measurement if performed under oxidising environment (in air or oxygen) or reduce the mass if performed under an inert environment. Fe-bearing hydrates also dehydroxylate to form hematite at higher temperatures. One of the major usages of TGA is determining the carbon content in fly ashes for consideration in concrete air entrainment, and the amount of carbon present in the fly ash can be under or over-estimated in ashes with high iron content [186] (Fig. 11). In iron-rich coal ashes, the hercynite phase ($FeAl_2O_4$) (stable at up to ~750 °C [187]) transforms into hematite and magnetite when heated to 960 °C in a quick burning process in an oxidising environment [188], whereas the magnetite phase already present in the ash transfers completely to hematite. The iron oxides in fly ash may also be reduced in an inert environment at high temperature (950 °C) as the organic carbon can oxidise to form CO_2 and reduce ferric oxide [189]. Iron sulfides or sulfates, generally present in iron corrosion products, and siderite can affect the TGA results as they form different products in multi-step reactions, especially in an oxidising environment [190,191]. Therefore, any samples with iron sulfides, sulfates or carbonates should be tested in an inert environment; and special care must be taken when interpreting TGA data if the sample has these compounds.

Iron often partially replaces aluminium in many hydrated phases such as monocarbonate, ettringite, and C-S-H, which affects the TGA results. Al-ettringite shows a minor mass loss peak in its DTG curve at around 250 °C, along with the major water loss peak between 30 and 150 °C; whereas Fe-ettringite only shows the major water loss peak and the minor bump at around 250 °C is not seen [38]. Similarly, Al-monocarbonate shows major DTG peaks at around 140 and 220 °C, whereas Fe-monocarbonate shows major peaks at around 170 and 240 °C [137].

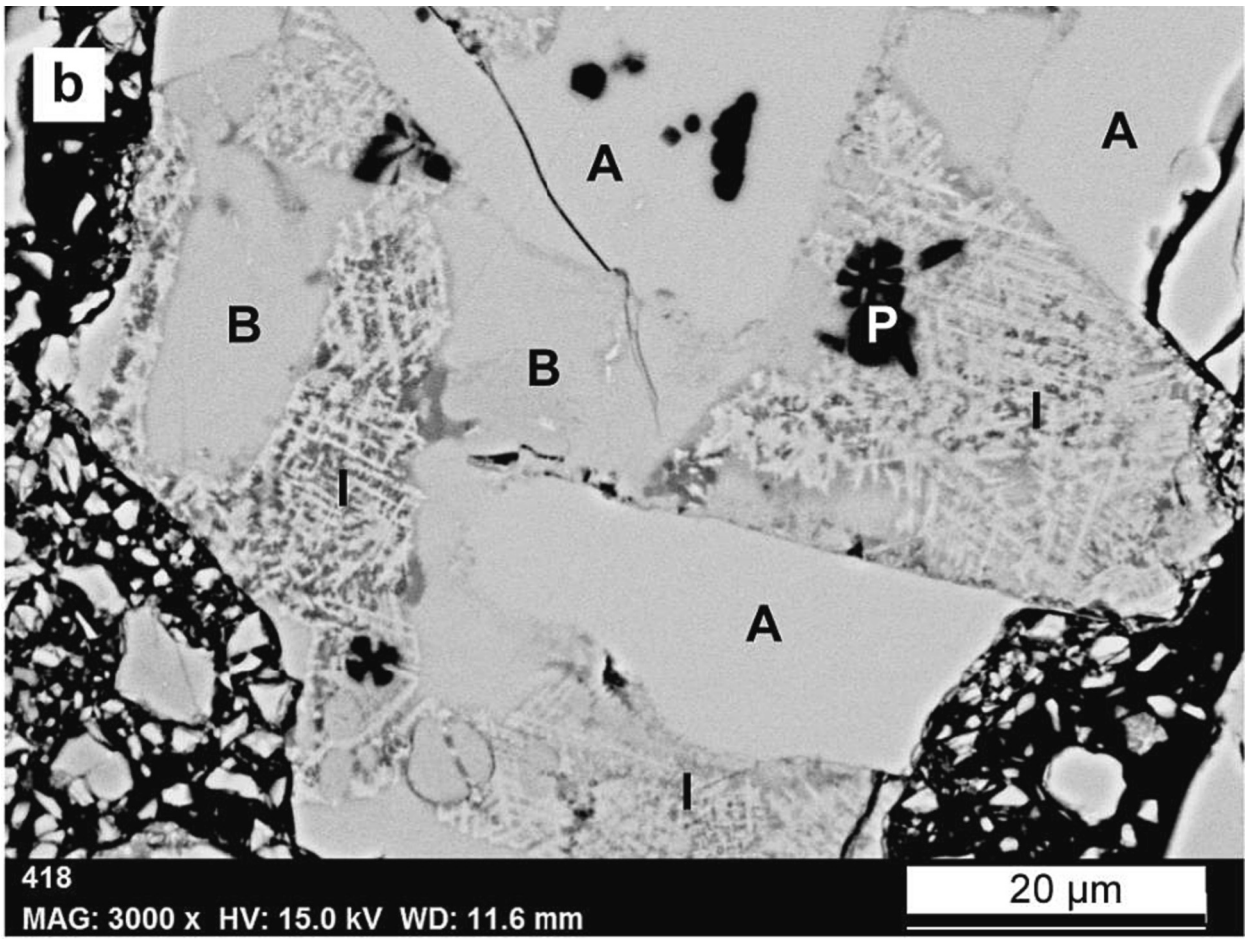

Fig. 10. Back-scattered electron micrograph of Portland clinker grain. A: alite, B: belite, P: periclase, I: interstitial phase showing dendritic ferrite [169] (reproduced with permission).

9. Laser diffraction particle size analysis

Laser diffraction is a commonly used technique for measuring particle size distribution of powder samples including different cementitious materials and precursors. Generally, the powder sample is dispersed in a fluid (generally isopropanol), and a laser light interacts with the dispersion upon which the intensity of the transmitted light and the angular distribution as well as the intensity of the scattered light is measured. The angular distribution is fitted using the Fraunhofer approximation if the particle sizes are much larger than the laser wavelength (generally 633 nm in most instruments) or Mie scattering theory if particle sizes are comparable to the laser wavelength (<25–50 µm) [203]. Applying the Mie scattering theory requires information regarding the complex refractive index, which includes the real refractive index and absorption coefficient (imaginary part) of both the particles and dispersing medium as input. Measuring the refractive index of powder samples through the Becke line test or the half-shadow test is a cumbersome procedure [204] and most of the literature uses reference values [205]. The particle sizes below 1–2 µm are specifically sensitive to the absorption coefficient [206–209] especially when the refractive index is <1.6. Even though there is no detailed study about variations in the complex refractive index of cementitious materials with iron content, it is well known that iron content affects the grey colour of cement, as well as is responsible for the brown or grey colour of fly ashes [210–213]. As such, the Fe content of a cementitious material may affect the complex refractive index, and thus affect the particle size distribution measured by laser diffraction techniques. This merits further attention in future studies.

10. Characterisation techniques mainly applied for solution phase analysis

Solution phase analysis in the cement chemistry field often involves the measurement of different ion concentrations in the aqueous phase to develop thermodynamical modelling of cement hydration, and/or studying the leaching behaviour of hardened concrete/cement paste for durability purposes. For pore-solution analysis of cementitious materials, the iron concentration is generally very low and is close to the iron concentration of a "blank" solution after the precipitation of ferrihydrites [214]; it may often be below the limit of detection (LoD). Moreover, in some cases, elemental compositions of cementitious materials are determined through a solution-phase analysis of the digested material instead of X-ray fluorescence, especially for light elements (atomic mass smaller than sodium) and elements that are present in trace quantities. The powder is generally digested in an acid (typically a combination of HNO_3, HCl, $HClO_4$ or HF, or others) [215] to convert the solid into a solution, but the presence of residue and the low recovery rate can cause errors [216–219]. Other digestion techniques include fluxing the powder with lithium tetraborate or lithium metaborate or a mix of the two borates and then dissolving the fused sample in HNO_3, which generally have a higher recovery rate than acid digestion methods [220,221]. Special care needs to be taken while fusing iron-rich samples in platinum crucibles, as iron may leach into the platinum crucible especially if it is present in metallic form [222,223], leading to an underestimation of iron content.

Major solution-based techniques for measuring elemental concentration include Inductively Coupled Plasma (ICP) techniques coupled

Table 6
Thermal decomposition and phase transformations of Fe-bearing minerals.

Phase name	Chemical formula	Mass change at different temperatures (°C)	Sample environment	Heating rate (°C/min) and testing environment	Reference
Goethite	α-FeO(OH)	Two-step mass loss from 196 to 224 and 263 to 282 resulted from dehydroxylation of goethite forming hematite. The high crystallinity of goethite is responsible for two peaks in DTG data. The temperature of mass loss increases with Al substitution.	Synthetic Al-substituted Goethite	TGA, 2 °C/min; 80 mL/min N_2 purging gas	[192]
		Goethite to hematite transformation at 275; structural hydroxide (in hematite) loss from 300 to 700	Synthetic goethite	TGA, 10 °C/min, in air	[193]
		Goethite to hematite transformation at 310; structural hydroxide loss (protohematite to hematite) from 300 to 700	Natural goethite ore	TGA, 10 °C/min, in air	[193]
Lepidocrocite	ɣ-FeO(OH)	Lepidocrocite forms maghemite through dehydroxylation between ~200 to ~275 (DTG peak at 255)	Synthetic samples with different degrees of crystallinity	TGA, 2 °C/min, in air	[194]
		Lepidocrocite forms maghemite through dehydroxylation between ~200 to ~275 (DTG peak at 242)	Synthetic sample	TGA, 4 °C/min, in argon	[195]
Magnetite	Fe_3O_4	100 % pure magnetite oxidises to form maghemite below 600. Magnetite converts to hematite completely when heated to 1000. If a hematite impurity is present in magnetite, magnetite converts directly to hematite.	Pure natural sample		[196]
Maghemite	ɣ-Fe_2O_3	At 550, maghemite converted to hematite. The transition temperature of nano-crystalline material is higher than a polycrystalline sample.	98 % pure maghemite	DTA, 10 °C/min	[197]
Wüstite	FeO	Stable at 400 for 24 h. Transferred completely to hematite when heated for 1 h at 600–700	Synthetic wüstite nanoparticles	Burning in a nitrogen environment	[198]
Ferrous and ferric sulfate	$FeSO_4$ and $Fe_2(SO_4)_3$	$FeSO_4$ and $Fe_2(SO_4)_3$ decompose to FeO and Fe_2O_3 respectively between 500 and 600	Synthetic reagent grade	TGA, 10 °C/min, 50 mL/min N_2 purging gas	[190]
Pyrite	FeS_2	Pyrite forms iron with a multi-step process pyrite → pyrrhotite → troilite → iron		Burning in an inert atmosphere	[191]
		Pyrite forms pyrrhotite, and then is converted to different iron oxides or sulfates depending on the burning temperature and oxygen concentration		Burning in an oxidising atmosphere	[191]
Siderite	$FeCO_3$	The decomposition path is siderite → magnetite → maghemite at 550; and siderite →wüstite + magnetite → magnetite → maghemite → hematite at 800	Siderite ore	Burning in a weak oxidising atmosphere	[199]
		Siderite → magnetite below 733 °C and siderite → wüstite + magnetite above 733 °C.	Siderite ore	Burning in an inert atmosphere (nitrogen)	[199]
2-Line ferrihydrite	$Fe_5HO_8{\cdot}4H_2O$, $5Fe_2O_3{\cdot}9H_2O$, or Fe_2O_3 ·2FeOOH·$2.6H_2O$	2-step mass loss 100–300 °C and another sharp peak between 350 and 450 depending on the synthesis procedure	Synthetic ferrihydrite	TGA, Air, 10 °C/min	[200]
		Heating up to ~220 increased structural order, at 325, it converts into α-Fe_2O_3	Synthetic ferrihydrite	Heating in air	[201]
Fe-containing Aft phase	$Ca_6[Al_{1-x}Fe_x(OH)_6]_2(SO_4)_3{\cdot}26H_2O$	Fe-containing ettringite loses water in between 30 and 150. A minor mass loss peak at around 250 observed in Al-ettringite is not found in Fe-containing ettringite.	Synthetic samples	TGA, N_2, 20 °C/min	[38]
Fe-containing hydrotalcite	$[Mg_{0.67}Fe_{0.33}(OH)_2](CO_3)_{0.165}{\cdot}0.57H_2O$	Dehydration occurs at around 100, followed by loss of CO_2 at around 400	Synthetic samples	TGA, 10 °C/min	[202]

with either Optical Emission Spectroscopy (OES), Atomic Emission Spectroscopy (AES) or Mass Spectroscopy (MS) detection, Ion Chromatography (IC), Atomic Absorption Spectroscopy (AAS), titration, and spectrophotometry. Among these methods, titration, IC and spectrophotometry can also be used for discriminating between Fe (II) and Fe (III) ion concentrations. The oxidation state of iron affects the solubility of different hydration phases, therefore information regarding Fe^{2+} and Fe^{3+} concentrations in the aqueous phase will enable accurate thermodynamic modelling of hydration product formation [137,224]. The oxidation state of iron in the aqueous phase is important for reinforced steel corrosion reactions [225]. Moreover, Fe^{2+} in solution takes part in the carbonation reaction by forming $FeCO_3$, whereas Fe^{3+} is not carbonated [226]. Further, the oxidation state of iron also affects the solubility of different hydration phases and information regarding Fe^{2+} and Fe^{3+} concentrations in the aqueous phase will enable accurate thermodynamic modelling of hydration product formation [137,224].

10.1. ICP techniques

ICP spectroscopy involves converting the solution sample into aerosol using a nebuliser, and then an ICP torch heats up the aerosol to subsequently convert it to particulate matter → atomic/ionic form → energised atomic or ionic form [227]. One of the major challenges with ICP techniques involves sample preparation at different dilution/concentration levels such that the concentration of the elements of interest is more than the limit of detection, but within the maximum calibration range. Further, there is a maximum allowed total dissolved solid content for ICP to ensure the nebuliser is not clogged, which makes measuring elements present in low quantities (which is often the case for iron in cementitious materials) challenging [228]. Other commonly present ions in cementitious materials samples such as Na and Ca in high concentration can also cause signal suppression leading to an underestimation of iron concentrations [229]. Calibrating the instrument with a matrix-matched standard solution or a series of spiked solutions is recommended for accurate Fe concentration measurement [230].

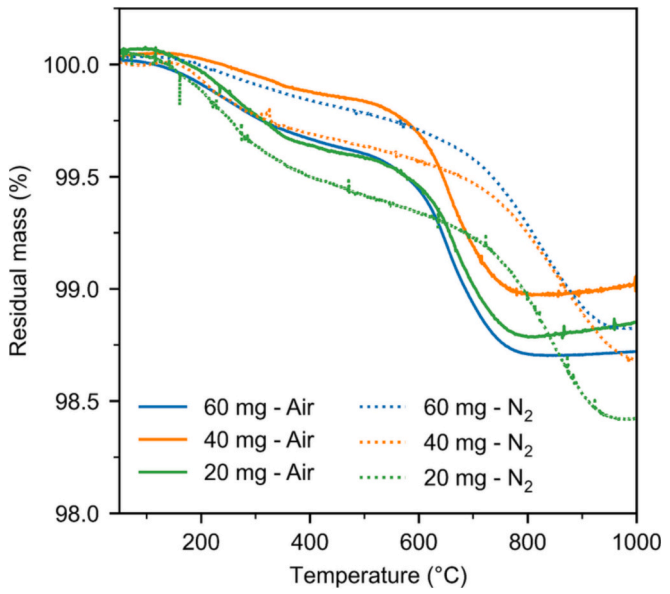

Fig. 11. Thermogravimetric analysis of a low-calcium, moderate-iron fly ash in air and nitrogen environment for different sample masses. The mass gain at higher temperature when the ash is heated in air corresponds to the oxidation of Fe^{2+}, which is not observed when heating in nitrogen. The purge gas flowrate is important in determining the oxidation kinetics and thus the mass change response at higher temperature.

The ICP-MS method involves using a mass spectrometer to identify different ions based on their atomic mass whereas ICP-OES and ICP-AES techniques detect the energy emitted from the energised atom using defined wavelengths. For determining Fe concentration, generally, a wavelength of 259.94 nm or 238.204 nm is chosen [231,232], depending on the other elements present. Using an MS detector provides a much lower LoD, but there can be spectral interferences from both isobaric overlap and polyatomic ions, created by the plasma excitation process. In general, ICP-MS is performed in an argon environment, and there are significant polyatomic ion interferences from $^{40}Ar^{16}O$ and $^{40}Ar^{16}O^{1}H$ for ^{56}Fe and ^{57}Fe, respectively [233]. Polyatomic interferences as well as a high total solid content in the cementitious materials sample make using ICP-MS quite challenging and most of the literature uses ICP-OES or ICP-AES over ICP-MS. More modern ICP-MS instruments can be equipped with helium collision mode coupled with kinetic energy discrimination (KED), which enables the breakdown of polyatomic species in a collision/reaction cell [234], thereby lowering the polyatomic interference. As most of the pore solutions, leachate or any other liquids in the cementitious materials field contain challenging-to-measure, complex ions, this capability is highly desirable for ICP-MS analysis.

Although ICP techniques are generally applied on solutions, laser ablation based ICP-MS (LA-IC-MS) or ICP-OES can be utilised on solid samples as well. The laser ablation technique consists of focussing a laser on a solid surface to generate very fine particles, which are then transported to an ICP-MS or ICP-OES instrument for elemental and isotope detection procedure. Recent development of femtosecond laser pulse sources has improved the sensitivity and accuracy of measurement, including iron, through reducing elemental/isotopic fractionation [235,236]. An LA-ICP-MS with a precision stage mover can create a 2D or 3D map of the elemental and isotopic composition of the solid sample, and such instruments have been used to map iron or ferroproteins in biological tissues [237], the different elements in clinker [238], as well as the extent of chloride and acid attacks in cementitious systems [239,240].

10.2. AAS

AAS analysis generally involves atomisation of a sample using either an air-acetylene (up to 2300 °C) or nitrous oxide-acetylene flame (up to 3000 °C) [241], or a graphite furnace (~3000 °C), followed by measurement of the absorbance of light of a particular wavelength defined by the element of interest (wavelength of 248.3 nm for Fe [242]). An air-acetylene flame is sufficient for iron measurements, as iron is relatively easier to atomise relative to refractory elements, e.g., aluminium, titanium etc., which require a higher temperature of the nitrous oxide-acetylene flame. A graphite furnace also allows running tests on slurries with total dissolved solids up to 20 %, because of nebulisers that are clogged at higher solid content are non-essential in a graphite furnace system and the higher atomisation efficiency of graphite furnace compared to the air-acetylene flame. This removes the errors associated with diluting samples and matrix effects that arise when using ICP techniques [243]. Capacho-Delgado and Manning measured the iron content of cement through a sodium carbonate fusion followed by hydrochloric acid digestion using a flame-based AAS [242]. AAS has also been used to measure the concentration of iron and other heavy metals in leaching tests [244] and in cement paste pore solution or aqueous phase [245].

10.3. Titration methods

Titration was used extensively for elemental quantification before the widespread availability of advanced characterisation equipment. There are multiple ways to measure iron content through titration – Pratt's method [246,247], the Zimmermann-Reinhardt method [248], 8-hydroxyquinoline titration [249], and EDTA titration [250]. ASTM C114 [251] describes the different titration methods for different elemental quantification of cements including iron. The cement is first dissolved either directly in HCl or after fusing with lithium metaborate, and then the iron in cement is reduced to Fe (II) using stannous chloride. The solution is subsequently titrated with potassium dichromate ($K_2Cr_2O_7$), with barium diphenyl sulfonate as an indicator, which turns purple at the titration point, providing the total iron content. For determining Fe(II) in a solid sample, the sample should be digested in acid in a sealed container to prevent oxidation of iron and then directly titrated using the method described above [252]. As the titration method is not extremely sensitive and is prone to human errors, it is not generally used in the recent scientific literature for measuring iron content in cement pore solution or aqueous phase and leachates, although it remains the ASTM reference method for cement analysis; EN 196-2 [253] specifies EDTA titration as the reference method, with XRF analysis as an accepted alternative procedure that is "equivalent" but "not fully validated" in the same way as the titration method.

The determination of Fe(II) by titration was recently used for determining the Fe(II)/Fe(III) ratio in fayalitic slags from non-ferrous metallurgy [254]. For these ferrous silicate glasses, a dissolution procedure using sulfuric and hydrofluoric acid was applied using an argon blanket. Titration with $Ce(SO_4)_2$ was carried out using a ferroin colour indicator (after neutralising the fluorine with H_3BO_3). Complete dissolution is necessary for success in this procedure, which can be complicated if, next to the ferrous silicate glass, spinel phases such as magnetite are present.

10.4. UV–visible spectroscopy

UV–visible-near infrared (UV–Vis-NIR) spectroscopy can be used to measure Fe^{2+} and Fe^{3+} concentrations in solution, using the Beer-Lambert principle that absorbance is directly proportional to concentration [255]. Measuring iron concentration using UV–Vis spectroscopy generally involves using a chromogenic compound that reacts with iron present in the solution and forms a complex with a high absorption coefficient at a particular wavelength in the UV–Vis-NIR range. One

Table 7
Summary of iron-rich cementitious materials characterisation techniques.

Technique	General principle	Sample type(s)	Comments/considerations
X-ray diffraction (XRD)	Diffraction of X-rays off crystallographic planes	Powder/monolith	Used for: quantitative phase analysis, crystal structure refinement or determination, PDF analysis, variable temperature measurements. Recommended use of Co X-ray source to reduce Fe fluorescence.
Neutron diffraction	Diffraction of neutrons after interaction with atoms nuclei	Powder/monolith	Used for: isotope substitution analysis, crystal structure refinement or determination, PDF analysis, positioning of light elements. Limitations: expensive neutron source, low signal-to-noise ratio. Complementary to XRD for fine structure refinements.
Pair distribution function (PDF)	Calculation of structure factor $S(Q)$ proportional to total scattered intensity I	Powder	Used for: structure analysis of short/medium-range order nano-crystalline and glassy materials.
Small-angle X-ray scattering (SAXS)	Elastic scattering of X-rays when travelling through material recorded at small angles: 0.1°–10°	Paste, colloidal suspension	Used for: microstructure and surface area evolution during setting and hardening, particle size and particle aggregation analysis. Limitations: tedious for multicomponent systems, background subtraction needed to account for Fe fluorescence.
Mössbauer spectroscopy (MS)	Measurement of nuclear recoil resulting from emission/absorption of gamma-rays	Powder/monolith, frozen solution	Adapted specifically for measuring ^{57}Fe by use of a ^{57}Co gamma-ray source. Used for studying Fe oxidation state, Fe coordination, local structure, and neighbouring atoms, presence of para−/ferromagnetism, crystallinity. Suitable for ex-situ kinetic studies. Limitations: long duration of measurements (up to 1 or few days).
Nuclear magnetic resonance (NMR)	Probes the magnetic moment of nuclei in a magnetic field	Powder, solution	NMR spectroscopy is used for: obtain information regarding the atomic structure and chemical environment around a particular element. ^{1}H NMR relaxometry is used to: obtain information regarding bulk structure, evaluate microstructure and porosity at different scales. Limitations: spectrometry difficult with high amounts of Fe^{3+} present due to paramagnetic effects.
Electronic paramagnetic/ferromagnetic resonance spectroscopy (EPR/FMR)	Analogous to NMR, whereby unpaired electrons are perturbed rather than nuclei	Powder, solution	Alternative to NMR, paramagnetism of Fe^{3+} is not an issue. Used for tracking chemical environment of Fe during setting.
X-ray absorption near-edge structure (XANES)	Fe atom is probed over the energy range required for electronic excitation of the K orbital (7.112 KeV) in the region on the K edge extending up to ~50 eV beyond	Powder/pellet (bulk), monolith/ thin section (μ-XAS)	Used for studying oxidation and coordination state of atoms, geometrical arrangement (bond angles) of neighbouring atoms.
Extended X-ray absorption fine structure (EXAFS)	Fe atom is probed beyond the K-edge and XANES region.	Powder/pellet (bulk), monolith/ thin section (μ-XAS)	Used for studying interatomic distances and coordination state of neighbouring atoms (nearest and next-nearest) with the aid of fitting models or by comparison with reference materials. Limitations: Fitting can be difficult in multiphase systems.
X-ray fluorescence (XRF)	Detection of fluorescent X-rays, after excitation of core electrons	Powder/bead; monolith/thin section for μ-XRF	Used for: average chemistry from the whole system (bulk), chemistry of specific regions (μ-XRF), surface element mapping.
Infrared (IR) spectroscopy	Measurement of IR light interacting with chemical bonds	Powder, solution	Fe-O bonds can be directly probed or the effect of the presence of Fe on the interaction of other bonds can be evaluated. Limitations: Fe—O bands can overlap with/have an effect on Si—O bands (predominant in cementitious systems). Can be used as a complementary technique on known samples.
Raman spectroscopy	Measurement of monochromatic visible, IR or UV lasers interacting with chemical bonds through inelastic scattering	Powder/monolith	Used for: often probing Fe—O bonds, identify the presence of Fe oxides and oxyhydroxides and other Fe minerals, studying the stoichiometry and Fe^{3+} substitution into Al^{3+} sites of ferrites. Limitations: low intensity, difficult to distinguish peaks from fluorescence background caused by iron-rich materials. To increase signal-to-noise ratio, samples can be washed with organic solvents, photobleached to reduce fluorescence, and immersed in low-fluorescence, high-refractive index immersion oil to reduce inter-particle scattering.
Optical microscopy	Observation of magnified features illuminated by visible light through lenses	Powder/monolith	Identify presence and spatial distribution of clinker phases.

(*continued on next page*)

Table 7 (*continued*)

Technique	General principle	Sample type(s)	Comments/considerations
Scanning electron microscopy (SEM) – Energy Dispersive X-ray Spectroscopy (EDX or EDS)	Detection of electrons and X-rays scattered off sample surface	Powder/monolith	Requires an accelerating voltage of >15 kV in order to quantify Fe. Monolith samples need to be well polished to obtain sufficiently accurate maps and element analysis.
Transmission electron microscopy (TEM) – Energy Dispersive X-ray Spectroscopy (EDX or EDS) – Electron Energy Loss Spectroscopy (EELS)	Detection of electrons and X-rays transmitted through sample	Ultrathin section	Samples are required to be sufficiently thin so that electrons can pass through. Can be a useful tool to investigate local oxidation states of iron.
Thermogravimetric analysis (TGA)	Weight change is measured against sample heating	Powder	Routinely used to quantify free and bound water content, hydration phases, carbonates, unburnt carbon, and sulfates. Fe-bearing minerals and oxides can oxidise and undergo phase changes during heating ramp.
Laser diffraction particle size analysis	Laser lights interact with dispersion and the intensity of transmitted and scattered light is proportional to the particle size.	Powder dispersed in liquid	Iron affects the refractive index required to measure particle size.
Inductively coupled plasma (ICP) spectroscopy	Sample is broken down in a plasma flame into charged ions, emitting at characteristic wavelength (ICP-OES) or ions are extracted into a mass spectrometer (ICP-MS)	Solution	Commonly present ions such as Na and Ca in high concentration can cause signal suppression in both ICP-OES and ICP-MS leading to underestimation of iron concentration
Atomic Absorption Spectroscopy (AAS)	Sample is atomised on a flame or furnace and absorbance of light at characteristic wavelengths is used to quantify elements	Solution	Iron is measured by the absorbance of light of wavelength 248.3 nm. Graphite furnace AAS does not generally suffer from sample matrix effects as ICP, thus providing accurate measurements without requiring complex matrix-matched calibration sample preparation.
Titration methods	Small increments of a reagent are added to the sample solution and a pH indicator shows the titration point	Solution	Used for measuring iron content, and Fe^{2+}/Fe^{3+} contents in solutions. Limitations: the method has limited sensitivity and is prone to human error, is becoming obsolete, replaced by more advanced characterisation techniques.
UV–visible spectroscopy	Transmitted light within a certain wavelength range is proportional to the concentration of a certain compound according to the Beer-Lambert's law	Solution	Used for measuring Fe^{2+} and Fe^{3+} concentration in solution. Chromogenic compounds can be reacted with iron to form a complex with high absorption coefficient at a particular wavelength in the UV–Vis-NIR range.
Ion chromatography (IC)	Ions in a solution are separated in an ion exchange resin column and identified based on their retention time	Solution	Used for quantification of anions. The separation technique is coupled with different detection methods, such as UV–Vis spectroscopy.

such compound is 1,10-phenanthroline which forms two different complexes with Fe^{2+} and Fe^{3+}, both of which are different in colour and can be used to quantify Fe^{2+} and Fe^{3+} concentration. The iron(II)-1,10-phenanthroline complex has [256] a peak absorbance wavelength at 512 nm with a reddish-orange colour; whereas the iron(III)-1,10-phenanthroline complex is yellowish with minimum absorbance at 512 nm. Further, the absorbance coefficient of both iron (II) and iron (III) complexes are exactly equal at 396 nm; thus both Fe^{2+} and Fe^{3+} concentrations can be quantified by measuring absorbance at 396 and 512 nm [256]. Perchloric acid also forms a ferric perchlorate complex, which has a peak absorbance wavelength at 240 nm, but absorbance at 260 nm is recommended because of lesser interference [257]. Recently, Cheng et al. [258] have proposed using a nitroso-R salt as the chemogenic compound along with cetyltrimethylammonium bromide (CTMAB) solution as a sensitiser and sodium iodide as a masking agent that removes interference from other ions, to measure the total iron concentration. The Fe-complex formed with nitroso-R salt has a peak absorption wavelength of 710 nm, and the detection limit of this technique can be as low as 4.5×10^{-8} M. Another chromogenic compound, the ferrozine reagent (monosodium salt hydrate of 3-(2-pyridyl)-5,6-diphenyl-1,2,4-triazine-p,p'-disulfonic acid) forms a complex with iron (II) with a peak absorbance wavelength at 562 nm in between pH 4 and 9 [259], and has recently been used to quantify iron-uptake in C-S-H [260].

10.5. Ion chromatography (IC)

IC generally involves binding the ions of interest to either a cation or anion exchange resin and then separating the ions of interest based on the elution order. The elution order depends on many factors including the polarisability of the ions, making the separation of ions of the same element but different oxidation states possible [261]. The concentration of the separated ions can be measured by different detection methods including UV–Vis spectrophotometry, chemiluminescence detection, conductance spectroscopy, or mass spectrometry [262]. In the field of cementitious materials, IC is generally used to measure the concentration of different anions, especially chloride and sulfates [263–265], whereas ICP-OES or AAS is used for cations. However, measurement of iron concentration using ion chromatography is regularly performed in biological, environmental, and geological samples [266–268] where knowledge about iron oxidation states is necessary for both solid and liquid samples. For example, Kanai digested geological materials samples using H_2SO_4 and HF and used pyridine-2,6-dicarboxylic acid (PDCA) as eluent and 4-(2-pyridylazo)resorcinol as the spectrophotometric reagent for simultaneous measurement of Cu^{2+}, Ni^{2+}, Zn^{2+}, Mn^{2+}, Fe^{2+}, and Fe^{3+}. The interference of other ions on Fe^{2+} and Fe^{3+} concentrations was minimal, but Fe^{2+} and Fe^{3+} content could be affected when the F^- concentration is higher than 0.25 M.

Different solution phase analysis methods have different advantages and disadvantages, but for cement pore solution or aqueous phase analysis, which potentially has the highest amount of interest in the field of cementitious materials, a very low limit of detection is necessary for measuring iron concentration. As such the ICP and AAS methods are the most practical ones to use, even if they are expensive. UV–Vis spectroscopy is a relatively inexpensive and in general easy to use characterisation technique, but more research is required to validate its usage in the field of cementitious materials.

11. Summary

Both common and advanced characterisation techniques that are particularly useful for characterising iron-containing phases in cementitious materials have been discussed in this paper and are summarised in Table 7.

In terms of the effects of iron on X-ray or neutron scattering techniques, the presence of iron in significant quantities can cause micro-absorption and fluorescence effects when using common Cu-anode X-ray sources. It is therefore recommended to use a different X-ray radiation source, such as Co or Mo, when analysing Fe-rich materials. The high scattering cross-section of iron may also hide signals from other elements, for instance in PDF measurements, and thus render the identification and assignments of scattering contributions beyond iron more tedious. Higher iron fluorescence is also known to affect SAXS data.

The presence of paramagnetic iron can cause peak broadening and changes in chemical shift and relaxation times in NMR experiments. Iron is also known to cause high fluorescence in Raman experiments, and using a different laser source wavelength may be required to reduce the fluorescence effects and collect useful Raman data. As the different iron-bearing minerals decompose at vastly different temperatures, performing routine TGA or DSC on cementitious samples will require detailed knowledge about different iron-bearing minerals present to obtain accurate phase quantification results.

Further to this, a few areas of research were identified that could enhance the accuracy and usability of characterisation techniques. First, a detailed study on the effect of different iron minerals and their quantities on the complex refractive index of cement and other cementitious materials would improve the particle size distribution of all cementitious materials measured by laser diffraction, a very common characterisation technique. Second, the development of easily accessible characterisation techniques for iron oxidation states is of interest, and of importance for thermodynamic modelling of clinkering and hydration processes. Mössbauer spectroscopy and X-ray absorption spectroscopy (XANES, EXAFS), and in some cases, X-ray PDF analysis, are well-developed and used in determining iron oxidation state or other structural information in solid samples. However, instruments required to perform most of these experiments are not commonly available, and laboratory-based X-ray absorption spectroscopy has not yet been applied to cements. Similarly, UV–Vis-NIR spectroscopy, ion chromatography, and titration methods are well-developed techniques used in other fields for understanding the iron oxidation state, but they still need to be refined and applied to characterise iron oxidation states in cement pore solution or aqueous phase and leaching tests. Further, the application of correlative characterisation and chemometrics can also improve the accuracy of the characterisation results in the field of cementitious materials, not just Fe-rich materials. Multi-scale imaging, advanced image segmentation techniques including using deep learning techniques for identifying different phases through BSE and optical image segmentation [269], quantification, and identification of phases from spectral data using principal component analysis etc. are relatively unexplored techniques in the field of cementitious materials [270]. Specifically for Fe-rich materials, X-ray PDF data analysis can be performed more accurately after combining information regarding the Fe oxidation state and coordination number obtained from XANES.

CRediT authorship contribution statement

Aniruddha Baral: Data curation, Investigation, Visualization, Writing – original draft, Writing – review & editing, Conceptualization, Formal analysis. **Cecilia Pesce:** Writing – original draft, Writing – review & editing, Investigation, Formal analysis. **Antonia S. Yorkshire:** Writing – original draft, Conceptualization, Writing – review & editing. **Zhanar Zhakiyeva:** Writing – original draft, Formal analysis, Investigation, Visualization. **Ruben Snellings:** Conceptualization, Investigation, Writing – original draft, Writing – review & editing, Supervision. **Theodore Hanein:** Conceptualization, Funding acquisition, Project administration, Resources, Supervision, Writing – review & editing, Writing – original draft. **John L. Provis:** Conceptualization, Funding acquisition, Project administration, Supervision, Visualization, Writing – original draft, Writing – review & editing, Resources. **Arne Peys:** Conceptualization, Data curation, Formal analysis, Investigation, Visualization, Writing – original draft, Writing – review & editing, Supervision.

Declaration of competing interest

The authors declare that they have no known competing financial interests or personal relationships that could have appeared to influence the work reported in this paper.

Data availability

Data will be made available on request.

Acknowledgements

T. Hanein was funded by the UKRI Future Leaders Fellowship (MR/V023829/1). A. Baral, C. Pesce, J. L. Provis, and T. Hanein were funded by EPSRC project EP/W018810/1, “Developing iron-rich cement clinker & understanding ferrite for the valorisation & upcycling of steel slags (FeRICH)”. J. L. Provis and A. S. Yorkshire were funded by EPSRC project EP/T013524/1, “Safe, efficient cementation of challenging radioactive wastes using alkali activated materials with high-flowability and high-anion retention capacity”. Dr. Sarah Kearney is acknowledged for the discussions regarding this paper.

Appendix A. Supplementary data

Supplementary data to this article can be found online at https://doi.org/10.1016/j.cemconres.2023.107419.

References

[1] A. Peys, V. Isteri, J. Yliniemi, A.S. Yorkshire, P.N. Lemougna, C. Utton, J. L. Provis, R. Snellings, T. Hanein, Sustainable iron-rich cements: raw material sources and binder types, Cem. Concr. Res. 157 (2022) 106834.
[2] Y. Elakneswaran, N. Noguchi, K. Matumoto, Y. Morinaga, T. Chabayashi, H. Kato, T. Nawa, Characteristics of ferrite-rich Portland cement: comparison with ordinary Portland cement, Front. Mater. 6 (2019) 97.
[3] K. Zhang, P. Shen, L. Yang, M. Rao, S. Nie, F. Wang, Development of high-ferrite cement: toward green cement production, J. Clean. Prod. 327 (2021) 129487.
[4] R. Gollop, H. Taylor, Microstructural and microanalytical studies of sulfate attack. II. Sulfate-resisting Portland cement: ferrite composition and hydration chemistry, Cem. Concr. Res. 24 (1994) 1347–1358.
[5] P.C. Hewlett, M.L. Liska, Lea’s Chemistry of Cement and Concrete, 5th ed., Butterworth-Heinemann, Elsevier, 2019.
[6] T.F. Newkirk, R.D. Thwaite, Pseudoternary system calcium oxide-monocalcium aluminate ($CaO{\cdot}Al_2O_3$)-dicalcium ferrite ($2CaO{\cdot}Fe_2O_3$), J. Res. Natl. Bur. Stand. 61 (1958) 233–245.
[7] W.C. Hansen, L.T. Brownmiller, R.H. Bogue, Studies on the system calcium oxide-alumina-ferric oxide, J. Am. Chem. Soc. 50 (1928) 396–406.
[8] P. Tarte, AI-Fe isomorphic substitution in $3CaO{\cdot}Al_2O_3$ and $2CaO.Fe_2O_3$, and interactions between the so-called C_3A and C_4AF phases, Nature 207 (1965) 973–974.
[9] H.F.W. Taylor, Cement Chemistry, Thomas Telford, London, 1997.
[10] M. Idrissi, A. Diouri, D. Damidot, J.M. Greneche, M.A. Talbi, M. Taibi, Characterisation of iron inclusion during the formation of calcium sulfoaluminate phase, Cem. Concr. Res. 40 (2010) 1314–1319.
[11] X. Huang, F. Wang, S. Hu, Y. Lu, M. Rao, Y. Mu, Brownmillerite hydration in the presence of gypsum: the effect of Al/Fe ratio and sulfate ions, J. Am. Ceram. Soc. 102 (2019) 5545–5554.
[12] Y. Tao, D. Wan, W. Zhang, F. Wang, S. Hu, Intrinsic reactivity and dissolution characteristics of tetracalcium aluminoferrite, Cem. Concr. Res. 146 (2021) 106485.
[13] J.S. Ndzila, S. Liu, G. Jing, S. Wang, Z. Ye, The effect of Fe^{3+} ion substitution on the crystal structure of ye’elimite, Ceramics-Silikáty 64 (2020) 18–28.
[14] N. Meller, C. Hall, J. Crawshaw, ESEM evidence for through-solution transport during brownmillerite hydration, J. Mater. Sci. 39 (2004) 6611–6614.

[15] J. Rose, A. Benard, S. El Mrabet, A. Masion, I. Moulin, V. Briois, L. Olivi, J. Y. Bottero, Evolution of iron speciation during hydration of C_4AF, Waste Manag. 26 (2006) 720–724.

[16] N. Noguchi, K. Siventhirarajah, T. Chabayashi, H. Kato, T. Nawa, Y. Elakneswaran, Hydration of ferrite-rich Portland cement: evaluation of Fe-hydrates and Fe uptake in calcium-silicate-hydrates, Constr. Build. Mater. 288 (2021) 123142.

[17] K.L. Aughenbaugh, P. Stutzman, M.C.G. Juenger, Identifying glass compositions in fly ash, Front. Mater. 3 (2016) 1.

[18] S.A. Bernal, V. Rose, J.L. Provis, The fate of iron in blast furnace slag particles during alkali-activation, Mater. Chem. Phys. 146 (2014) 1–5.

[19] V. Hallet, M.T. Pedersen, B. Lothenbach, F. Winnefeld, N. De Belie, Y. Pontikes, Hydration of blended cement with high volume iron-rich slag from non-ferrous metallurgy, Cem. Concr. Res. 151 (2022) 106624.

[20] C. Siakati, A.P. Douvalis, V. Hallet, A. Peys, Y. Pontikes, Influence of CaO/FeO ratio on the formation mechanism and properties of alkali-activated Fe-rich slags, Cem. Concr. Res. 146 (2021) 106466.

[21] E. Bernard, B. Lothenbach, C. Chlique, M. Wyrzykowski, A. Dauzères, I. Pochard, C. Cau-Dit-Coumes, Characterization of magnesium silicate hydrate (M-S-H), Cem. Concr. Res. 116 (2019) 309–330.

[22] A. Peys, A.P. Douvalis, V. Hallet, H. Rahier, B. Blanpain, Y. Pontikes, Inorganic polymers from CaO-FeO_x-SiO_2 slag: the start of oxidation of Fe and the formation of a mixed valence binder, Front. Mater. 6 (2019) 212.

[23] B. Lothenbach, P. Durdziński, K. De Weerdt, Thermogravimetric analysis, in: K. Scrivener, R. Snellings, B. Lothenbach (Eds.), A Practical Guide to Microstructural Analysis of Cementitious Materials, CRC Press, Boca Raton FL, 2016, pp. 1–36.

[24] A. Peys, A.P. Douvalis, C. Siakati, H. Rahier, B. Blanpain, Y. Pontikes, The influence of air and temperature on the reaction mechanism and molecular structure of Fe-silicate inorganic polymers, J. Non-Cryst. Solids 526 (2019) 119675.

[25] A. Peys, C.E. White, D. Olds, H. Rahier, B. Blanpain, Y. Pontikes, Molecular structure of CaO–FeO_x–SiO_2 glassy slags and resultant inorganic polymer binders, J. Am. Ceram. Soc. 101 (2018) 5846–5857.

[26] S. Simon, G.J.G. Gluth, A. Peys, S. Onisei, D. Banerjee, Y. Pontikes, The fate of iron during the alkali-activation of synthetic (CaO-)FeO_x-SiO_2 slags: an Fe K-edge XANES study, J. Am. Ceram. Soc. 101 (2018) 2107–2118.

[27] S. Onisei, A.P. Douvalis, A. Malfliet, A. Peys, Y. Pontikes, Inorganic polymers made of fayalite slag: on the microstructure and behavior of Fe, J. Am. Ceram. Soc. 101 (2018) 2245–2257.

[28] R. Snellings, X-ray powder diffraction applied to cement, in: K. Scrivener, R. Snellings, B. Lothenbach (Eds.), A Practical Guide to Microstructural Analysis of Cementitious Materials, CRC Press, Boca Raton FL, 2016, pp. 107–176.

[29] R.T. Downs, M. Hall-Wallace, The American Mineralogist crystal structure database, Am. Mineral. 88 (2003) 247–250.

[30] S. Gražulis, D. Chateigner, R.T. Downs, A. Yokochi, M. Quirós, L. Lutterotti, E. Manakova, J. Butkus, P. Moeck, A. Le Bail, Crystallography Open Database–an open-access collection of crystal structures, J. Appl. Crystallogr. 42 (2009) 726–729.

[31] L.W. Finger, R.M. Hazen, Crystal structure and isothermal compression of Fe_2O_3, Cr_2O_3, and V_2O_3 to 50 kbars, J. Appl. Phys. 51 (1980) 5632–5637.

[32] B.A. Wechsler, D.H. Lindsley, C.T. Prewit, Crystal structure and cation distribution in titanomagnetites ($Fe_{3-x}Ti_xO_4$), Am. Mineral. 69 (1984) 754–770.

[33] A. Yamamoto, Modulated structure of wustite ($Fe_{1-x}O$) (three-dimensional modulation), Acta Crystallogr. B 38 (1982) 1451–1456.

[34] H.S.C. O'Neill, H. Annersten, D. Virgo, The temperature dependence of the cation distribution in magnesioferrite ($MgFe_2O_4$) from powder XRD structural refinements and Mössbauer spectroscopy, Am. Mineral. 77 (1992) 725–740.

[35] G.J. Redhammer, G. Tippelt, G. Roth, G. Amthauer, Structural variations in the brownmillerite series: single-crystal X-ray diffraction at 25 °C and high temperature X-ray powder diffraction (25 °C ≤ T ≤ 1000 °C), Am. Mineral. 89 (2004) 405–420.

[36] B.Z. Dilnesa, Fe-containing hydrates and their fate during cement hydration: Thermodynamic data and experimental study, Ecole Polytechnique Fédérale de Lausanne, Switzerland, 2011.

[37] B.Z. Dilnesa, B. Lothenbach, G. Renaudin, A. Wichser, E. Wieland, H. Jennings, Stability of monosulfate in the presence of iron, J. Am. Ceram. Soc. 95 (2012) 3305–3316.

[38] G. Möschner, B. Lothenbach, F. Winnefeld, A. Ulrich, R. Figi, R. Kretzschmar, Solid solution between Al-ettringite and Fe-ettringite ($Ca_6[Al_{1-x}Fe_x(OH)_6]_2(SO_4)_3{\cdot}26H_2O$), Cem. Concr. Res. 39 (2009) 482–489.

[39] H.M. Rietveld, A profile refinement method for nuclear and magnetic structures, J. Appl. Crystallogr. 2 (1969) 65–71.

[40] B.E. Warren, X-ray Diffraction, Dover Publications, New York NY, 1990.

[41] G.W. Brindley, XLV., The effect of grain or particle size on x-ray reflections from mixed powders and alloys, considered in relation to the quantitative determination of crystalline substances by X-ray methods, Lond. Edinb. Dublin Philos. Mag. J. Sci. 36 (1945) 347–369.

[42] G. Le Saoût, V. Kocaba, K. Scrivener, Application of the Rietveld method to the analysis of anhydrous cement, Cem. Concr. Res. 41 (2011) 133–148.

[43] M.A.G. Aranda, A.G. De la Torre, L. León-Reina, Powder-diffraction characterisation of cements, International Tables for Crystallography (2019) 855–867.

[44] B.Z. Dilnesa, B. Lothenbach, G. Renaudin, A. Wichser, D. Kulik, Synthesis and characterization of hydrogarnet $Ca_3(Al_xFe_{1-x})_2(SiO_4)_y(OH)_{4(3-y)}$, Cem. Concr. Res. 59 (2014) 96–111.

[45] E. Woermann, W. Eysel, T. Hahn, Polymorphism and solid solution of the ferrite phase, 5th International Symposium on the Chemistry of Cement, Tokyo, Part I, 1968, pp. 54–60.

[46] V. Kahlenberg, R.X. Fischer, C.S.J. Shaw, Rietveld analysis of dicalcium aluminate ($Ca_2Al_2O_5$)—a new high pressure phase with the Brownmillerite-type structure, Am. Mineral. 85 (2000) 1061–1065.

[47] A.A. Colville, S. Geller, The crystal structure of brownmillerite, Ca_2FeAlO_5, Acta Crystallogr. B 27 (1971) 2311–2315.

[48] A.A. Colville, The crystal structure of $Ca_2Fe_2O_6$ and its relation to the nuclear electric field gradient at the iron sites, Acta Crystallogr. B 26 (1970) 1469–1473.

[49] V. Peterson, B. Hunter, A. Ray, L.P. Aldridge, Rietveld refinement of neutron, synchrotron and combined powder diffraction data of cement clinker, Appl. Phys. A 74 (2002) s1409–s1411.

[50] A.C. Jupe, J.K. Cockcroft, P. Barnes, S.L. Colston, G. Sankar, C. Hall, The site occupancy of Mg in the brownmillerite structure and its effect on hydration properties: an X-ray/neutron diffraction and EXAFS study, J. Appl. Crystallogr. 34 (2001) 55–61.

[51] E. Lorch, Neutron diffraction by germania, silica and radiation-damaged silica glasses, J. Phys. C Solid State Phys. 2 (1969) 229–237.

[52] A.K. Soper, GudrunN and GudrunX: programs for correcting raw neutron and X-ray diffraction data to differential scattering cross section, Science & Technology Facilities Council, Swindon, UK, 2011. Technical Report RAL-TR-2011-013.

[53] X. Qiu, J.W. Thompson, S.J. Billinge, PDFgetX2: a GUI-driven program to obtain the pair distribution function from X-ray powder diffraction data, J. Appl. Crystallogr. 37 (2004) 678.

[54] W.H. McMaster, N.K. Del Grande, J.H. Mallett, J.H. Hubbell, Compilations of X-ray Cross Sections, UCRL-50174 Sec, University of California, Livermore CA, II Rev. I, 1969.

[55] V.F. Sears, Neutron scattering lengths and cross sections, Neutron News 3 (1992) 26–37.

[56] A. Peys, C.E. White, H. Rahier, B. Blanpain, Y. Pontikes, Alkali-activation of CaO-FeO_x-SiO_2 slag: formation mechanism from in-situ X-ray total scattering, Cem. Concr. Res. 122 (2019) 179–188.

[57] K. Gong, C.E. White, Impact of chemical variability of ground granulated blast-furnace slag on the phase formation in alkali-activated slag pastes, Cem. Concr. Res. 89 (2016) 310–319.

[58] C. Siakati, R. Macchieraldo, B. Kirchner, F. Tielens, A. Peys, D. Seveno, Y. Pontikes, Unraveling the nano-structure of a glassy CaO-FeO-SiO_2 slag by molecular dynamics simulations, J. Non-Cryst. Solids 528 (2020) 119771.

[59] K. Gong, C.E. White, Predicting CaO-(MgO)-Al_2O_3-SiO_2 glass reactivity in alkaline environments from force field molecular dynamics simulations, Cem. Concr. Res. 150 (2021) 106588.

[60] I. Maruyama, N. Sakamoto, K. Matsui, G. Igarashi, Microstructural changes in white Portland cement paste under the first drying process evaluated by WAXS, SAXS, and USAXS, Cem. Concr. Res. 91 (2017) 24–32.

[61] G. Porod, Die Röntgenkleinwinkelstreuung von dichtgepackten kolloiden Systemen, Kolloid-Zeitschrift 124 (1951) 83–114.

[62] A. Guinier, G. Fournet, Small-Angle Scattering of X-rays (trans. C.B. Walker),, John Wiley & Sons, New York NY, 1955.

[63] I. Maruyama, G. Igarashi, K. Matsui, N. Sakamoto, Hinderance of C-S-H sheet piling during first drying using a shrinkage reducing agent: a SAXS study, Cem. Concr. Res. 144 (2021) 106429.

[64] A. Baral, E. Tajuelo Rodriguez, W.A. Hunnicutt, E. Cakmak, H. Sun, J. Ilavsky, Y. Le Pape, T.M. Rosseel, N. Garg, Ultra-high gamma irradiation of calcium silicate hydrates: impact on mechanical properties, nanostructure, and atomic environments, Cem. Concr. Res. 158 (2022) 106855.

[65] J.J. Thomas, H.M. Jennings, A.J. Allen, The surface area of hardened cement paste as measured by various techniques, Concr. Sci. Eng. 1 (1999) 45–64.

[66] A.J. Allen, J.J. Thomas, H.M. Jennings, Composition and density of nanoscale calcium–silicate–hydrate in cement, Nat. Mater. 6 (2007) 311–316.

[67] A. Masion, E. Doelsch, J. Rose, S. Moustier, J.Y. Bottero, P.M. Bertsch, Speciation and crystal chemistry of iron(III) chloride hydrolyzed in the presence of SiO_4 ligands : Semilocal scale structure of the aggregates, Langmuir 17 (2001) 4753–4757.

[68] L. Melníková, V.I. Petrenko, M.V. Avdeev, V.M. Garamus, L. Almásy, O.I. Ivankov, L.A. Bulavin, Z. Mitróová, P. Kopčanský, Effect of iron oxide loading on magnetoferritin structure in solution as revealed by SAXS and SANS, Colloids Surf. B: Biointerfaces 123 (2014) 82–88.

[69] A. Beauvois, D. Vantelon, J. Jestin, A. Dupont, V. Briois, E. Paineau, T. Bizien, A. Pradel, M. Davranche, Aluminum-induced colloidal destabilization of iron-organic matter nanoaggregates, Geochim. Cosmochim. Acta 344 (2023) 1–11.

[70] M. Bonini, E. Fratini, P. Baglioni, SAXS study of chain-like structures formed by magnetic nanoparticles, Mater. Sci. Eng. C 27 (2007) 1377–1381.

[71] A.B.G.M. Leferink op Reinink, E. van den Pol, G.J. Vroege, A.V. Petukhov, SAXS reveals the magnetic alignment pathway of the goethite columnar liquid crystal phase, J. Colloid Interface Sci. 428 (2014) 316–320.

[72] M. Kriechbaum, G. Degovics, P. Laggner, J. Tritthart, Investigations on cement pastes by small-angle X-ray scattering and BET: the relevance of fractal geometry, Adv. Cem. Res. 6 (1994) 93–101.

[73] J.M.D. Coey, Mössbauer spectroscopy of silicate minerals, in: G.J. Long (Ed.), Mössbauer Spectroscopy Applied to Inorganic Chemistry, Plenum Press, New York NY, 1984, pp. 443–509.

[74] N.N. Greenwood, T.C. Gibb, Mössbauer Spectroscopy, Springer, Dordrecht, 1971.

[75] G.M. Bancroft, A.G. Maddock, R.G. Burns, Applications of the Mössbauer effect to silicate mineralogy—I. Iron silicates of known crystal structure, Geochim. Cosmochim. Acta 31 (1967) 2219–2246.

[76] R.G. Burns, T.C. Solberg, ^{57}Fe-bearing oxide, silicate, and aluminosilicate minerals, spectroscopic characterization of minerals and their surfaces, American Chemical Society Symposium Series 415 (1990) 262–283.

[77] A.A. Kamnev, R.L. Dykman, K. Kovács, A.N. Pankratov, A.V. Tugarova, Z. Homonnay, E. Kuzmann, Redox interactions between structurally different alkylresorcinols and iron(III) in aqueous media: frozen-solution ^{57}Fe Mössbauer spectroscopic studies, redox kinetics and quantum chemical evaluation of the alkylresorcinol reactivities, Struct. Chem. 25 (2014) 649–657.

[78] C. Krebs, J.C. Price, J. Baldwin, L. Saleh, M.T. Green, J.M. Bollinger, Rapid freeze-quench ^{57}Fe Mössbauer spectroscopy: monitoring changes of an iron-containing active site during a biochemical reaction, Inorg. Chem. 44 (2005) 742–757.

[79] K.T. Douglas, B. Howlin, J. Silver, Solution chemistry and Mössbauer study of iron(II) and iron(III) complexes from gallocyanine, Inorg. Chim. Acta 92 (1984) 135–140.

[80] J. Silver, I.E.G. Morrison, L.V.C. Rees, A Mössbauer spectroscopic study of frozen solutions of $FeCl_3$ — phenols, Inorg. Nucl. Chem. Lett. 15 (1979) 433–436.

[81] A.P. Douvalis, A. Polymeros, T. Bakas, IMSG09: a ^{57}Fe-^{119}Sn Mössbauer spectra computer fitting program with novel interactive user interface, J. Phys. Conf. Ser. 217 (2010) 012014.

[82] B. Wareppam, E. Kuzmann, V.K. Garg, L.H. Singh, Mössbauer spectroscopic investigations on iron oxides and modified nanostructures: a review, J. Mater. Res. 38 (2023) 937–957.

[83] R.G. Burns, Mineral Mössbauer spectroscopy: correlations between chemical shift and quadrupole splitting parameters, Hyperfine Interact. 91 (1994) 739–745.

[84] M.Y. Hassaan, N.A. Eissa, Applications of Mössbauer spectroscopy in cement studies, Ceram. Bull. 66 (12) (1986) 73–81.

[85] Z. Yanwei, Y. Nanru, A comparative study of the ferritephase in high-iron cements with the pure $C_2A_xF_{1-X}$ by Mössbauer spectroscopy, Cem. Concr. Res. 21 (1991) 31–37.

[86] H.K. Choudhary, A.V. Anupama, R. Kumar, M.E. Panzi, S. Matteppanavar, B. N. Sherikar, B. Sahoo, Observation of phase transformations in cement during hydration, Constr. Build. Mater. 101 (2015) 122–129.

[87] F.D. Tamás, A. Vértes, A Mössbauer study on the hydration of brownmillerite ($4CaO{\cdot}Al_2O_3{\cdot}Fe_2O_3$), Cem. Concr. Res. 3 (1973) 575–581.

[88] Q.E. Stahl, G.J. Redhammer, G. Tippelt, A. Reyer, Structural and spectroscopic characterization of the brownmillerite-type $Ca_2Fe_{2-x}Ga_xO_5$ solid solution series, Phys. Chem. Miner. 46 (2019) 271–298.

[89] K.S. Harchand, R. Kumar, K. Chandra, Vishwamittar, Mössbauer and X-ray investigations of some Portland cements, Cem. Concr. Res. 14 (1984) 170–176.

[90] P.G. de la Iglesia, O. García-Moreno, J.L. Menéndez, R. Torrecillas, J.F. Marco, Exploring the limits of Fe^{3+} solid solution in calcium hexaluminate, J. Mater. Res. 38 (2023) 1129–1137.

[91] V. Lilkov, O. Petrov, Y. Tzvetanova, P. Savov, M. Kadiyski, Mössbauer, XRD, and complex thermal analysis of the hydration of cement with fly ash, J. Spectrosc. 2013 (2013) 231843.

[92] B. Walkley, J.L. Provis, Solid-state nuclear magnetic resonance spectroscopy of cements, Mater. Today Adv. 1 (2019) 100007.

[93] K.J.D. Mackenzie, M.E. Smith, Multinuclear Solid-state NMR of Inorganic Materials, Pergamon, Oxford, 2002.

[94] A.M. Gajewicz-Jaromin, P.J. McDonald, A.C.A. Muller, K.L. Scrivener, Influence of curing temperature on cement paste microstructure measured by ^{1}H NMR relaxometry, Cem. Concr. Res. 122 (2019) 147–156.

[95] S.M. Nagel, C. Strangfeld, S. Kruschwitz, Application of ^{1}H proton NMR relaxometry to building materials – a review, J. Magn. Reson. Open 6-7 (2021) 100012.

[96] M. Wyrzykowski, A.M. Gajewicz-Jaromin, P.J. McDonald, D.J. Dunstan, K. L. Scrivener, P. Lura, Water redistribution–microdiffusion in cement paste under mechanical loading evidenced by ^{1}H NMR, J. Phys. Chem. C 123 (2019) 16153–16163.

[97] S. Gomes, M. François, Characterization of mullite in silicoaluminous fly ash by XRD, TEM, and ^{29}Si MAS NMR, Cem. Concr. Res. 30 (2000) 175–181.

[98] D.A. Netzel, Multinuclear NMR approach to coal fly ash characterization, U.S. Department of, Energy Report DE-FC21-86MC11076 (1991).

[99] P.A. Schroeder, R.J. Pruett, V.J. Hurst, Effects of secondary iron phases on kaolinite ^{27}Al MAS NMR spectra, Clay Clay Miner. 46 (1998) 429–435.

[100] J. Skibsted, E. Henderson, H.J. Jakobsen, Characterisation of calcium aluminate phases in cements by ^{27}Al MAS NMR spectroscopy, Inorg. Chem. 32 (1993) 1013–1027.

[101] J. Skibsted, H.J. Jakobsen, C. Hall, Quantitative aspects of ^{27}Al MAS NMR of calcium aluminoferrites, Adv. Cem. Based Mater. 7 (1998) 57–59.

[102] C.L. Edwards, L.B. Alemany, A.R. Barron, Solid-state ^{29}Si NMR analysis of cements: comparing different methods of relaxation analysis for determining spin-lattice relaxation times to enable determination of the C_3S/C_2S ratio, Ind. Eng. Chem. Res. 46 (2007) 5122–5130.

[103] S.L. Poulsen, V. Kocaba, G. Le Saout, H.J. Jakobsen, K.L. Scrivener, J. Skibsted, Improved quantification of alite and belite in anhydrous Portland cements by ^{29}Si MAS NMR: effects of paramagnetic ions, Solid State Nucl. Magn. Reson. 36 (2009) 32–44.

[104] A. Rawal, B.J. Smith, G.L. Athens, C.L. Edwards, L. Roberts, V. Gupta, B. F. Chmelka, Molecular silicate and aluminate species in anhydrous and hydrated cements, J. Am. Chem. Soc. 132 (2010) 7321–7337.

[105] H. Hilbig, F.H. Köhler, P. Schießl, Quantitative ^{29}Si MAS NMR spectroscopy of cement and silica fume containing paramagnetic impurities, Cem. Concr. Res. 36 (2006) 326–329.

[106] J.P. Korb, M. Whaley-Hodges, R.G. Bryant, Translational diffusion of liquids at surfaces of microporous materials: theoretical analysis of field-cycling magnetic relaxation measurements, Phys. Rev. E 56 (1997) 1934–1945.

[107] R.M.E. Valckenborg, L. Pel, K. Kopinga, NMR relaxation and diffusion measurements on ion(III)-doped kaolin clay, J. Magn. Reson. 151 (2001) 291–297.

[108] A. Valori, P.J. McDonald, K.L. Scrivener, The morphology of C–S–H: Lessons from ^{1}H nuclear magnetic resonance relaxometry, Cem. Concr. Res. 49 (2013) 65–81.

[109] R. Schulte Holthausen, M. Raupach, A phenomenological approach on the influence of paramagnetic iron in cement stone on 2D T_1-T_2 relaxation in single-sided ^{1}H nuclear magnetic resonance, Cem. Concr. Res. 120 (2019) 279–293.

[110] C. Cadar, A. Cretu, M. Moldovan, C. Mattea, S. Stapf, I. Ardelean, NMR T_1–T_2 correlation analysis of molecular absorption inside a hardened cement paste containing silanised silica fume, Mol. Phys. 117 (2019) 1000–1005.

[111] M.R.J. Carroll, K. O'Neill, N.W. Bristow, T. Hopper, S.J. Vogt, M.L. Johns, E. O. Fridjonsson, NMR derived water content from high magnetic susceptibility rock cuttings, Miner. Eng. 122 (2018) 211–219.

[112] Z. Yu, R. de Oliveira-Silva, Y. Pontikes, D. Sakellariou, Low-field ^{1}H NMR study on geopolymers: the effect of paramagnetic Fe(III), Cem. Concr. Res. 166 (2023) 107116.

[113] D. Govindarajan, R. Gopalakrishnan, P.S. Rao, Electron paramagnetic resonance study on metakaolin-admixtured cement paste at different hydrated periods, Radiat. Eff. Defects Solids 163 (2008) 795–804.

[114] N. Guskos, M. Sobon, A. Guskos, J. Typek, I.E. Lipinski, K. Aidinis, J. Blyszko, W. Kiernozycki, U. Narkiewicz, M. Podsiadly, Ageing effect in carbon-coated cobalt nanoparticles embedded in a cement matrix studied by FMR, Rev. Adv. Mater. Sci. 14 (2007) 130–134.

[115] N. Guskos, G. Zolnierkiewicz, A. Guskos, J. Typek, J. Blyszko, W. Kiernozycki, U. Narkiewicz, M. Podsiadly, Magnetic properties of the micro-silica/cement matrix with carbon-coated cobalt nanoparticles and free radical DPPH, J. Non-Cryst. Solids 354 (2008) 4510–4514.

[116] L. Lapcik, Z. Simek, Electron paramagnetic resonance study of dry cements, Cem. Concr. Res. 26 (1996) 237–242.

[117] J. Siramanont, B.J. Walder, L. Emsley, P. Bowen, Iron incorporation in synthetic precipitated calcium silicate hydrates, Cem. Concr. Res. 142 (2021) 106365.

[118] C.R. Kaze, G.L. Lecomte-Nana, E. Kamseu, P.S. Camacho, A.S. Yorkshire, J. L. Provis, M. Duttine, A. Wattiaux, U.C. Melo, Mechanical and physical properties of inorganic polymer cement made of iron-rich laterite and lateritic clay: a comparative study, Cem. Concr. Res. 140 (2021) 106320.

[119] S. Calvin, XAFS for Everyone, Taylor & Francis CRC Press, Boca Raton, 2013.

[120] J. Als-Nielsen, D. McMorrow, Elements of Modern X-ray Physics, 2nd ed., Wiley, New York NY, 2011.

[121] L.M. Mottram, S. Cafferkey, A.R. Mason, T. Oulton, S.K. Sun, D.J. Bailey, M. C. Stennett, N.C. Hyatt, A feasibility investigation of speciation by Fe K-edge XANES using a laboratory X-ray absorption spectrometer, J. Geosci. 65 (2020) 27–35.

[122] C.M.B. Henderson, G. Cressey, S.A.T. Redfern, Geological applications of synchrotron radiation, Radiat. Phys. Chem. 45 (1995) 459–481.

[123] A. Mancini, B. Lothenbach, G. Geng, D. Grolimund, D.F. Sanchez, S.C. Fakra, R. Dähn, B. Wehrli, E. Wieland, Iron speciation in blast furnace slag cements, Cem. Concr. Res. 140 (2021) 106287.

[124] B. Ravel, M. Newville, ATHENA, ARTEMIS, HEPHAESTUS: data analysis for X-ray absorption spectroscopy using IFEFFIT, J. Synchrotron Radiat. 12 (2005) 537–541.

[125] L. Galoisy, G. Calas, M.A. Arrio, High-resolution XANES spectra of iron in minerals and glasses: structural information from the pre-edge region, Chem. Geol. 174 (2001) 307–319.

[126] M. Wilke, F. Farges, P.-E. Petit, G.E. Brown Jr., F. Martin, Oxidation state and coordination of Fe in minerals: an Fe K-XANES spectroscopic study, Am. Mineral. 86 (2001) 714–730.

[127] G. Giuli, G. Pratesi, C. Cipriani, E. Paris, Iron local structure in tektites and impact glasses by extended X-ray absorption fine structure and high-resolution X-ray absorption near-edge structure spectroscopy, Geochim. Cosmochim. Acta 66 (2002) 4347–4353.

[128] B. Ma, A. Fernandez-Martinez, A. Mancini, B. Lothenbach, Spectroscopic investigations on structural incorporation pathways of Fe^{III} into zeolite frameworks in cement-relevant environments, Cem. Concr. Res. 140 (2021) 106304.

[129] T. Vehmas, V. Montoya, M.C. Alonso, R. Vašíček, E. Rastrick, S. Gaboreau, P. Večerník, M. Leivo, E. Holt, N. Fink, N. Ait Mouheb, J. Svoboda, D. Read, R. Červinka, R. Vasconcelos, C. Corkhill, Characterization of Cebama low-pH reference concrete and assessment of its alteration with representative waters in radioactive waste repositories, Appl. Geochem. 121 (2020) 104703.

[130] A. Cheniour, Y. Li, J. Sanahuja, Y. Le Pape, E. Tajuelo Rodriguez, L.M. Anovitz, K. C. Polavaram, N. Garg, T.M. Rosseel, FFT-based model for irradiated aggregate microstructures in concrete, Mater. Struct. 55 (2022) 214.

[131] M.K. Moradllo, B. Sudbrink, Q. Hu, M. Aboustait, B. Tabb, M.T. Ley, J.M. Davis, Using micro X-ray fluorescence to image chloride profiles in concrete, Cem. Concr. Res. 92 (2017) 128–141.

[132] S. Chinchón-Payá, A. Aguado, F. Coloma, S. Chinchón, Study of aggregate samples with iron sulfides through micro X-ray fluorescence (μXRF) and X-ray photoelectron spectroscopy (XPS), Mater. Struct. 48 (2015) 1285–1290.

[133] J.L. Provis, V. Rose, S.A. Bernal, J.S.J. van Deventer, High-resolution nanoprobe x-ray fluorescence characterization of heterogeneous calcium and heavy metal distributions in alkali-activated fly ash, Langmuir 25 (2009) 11897–11904.

[134] B.H. Stuart, Infrared Spectroscopy: Fundamentals and Applications, Wiley, Chichester, England, 2004.
[135] S.P. Varma, E. Henderson, C.D. Wall, The application of low temperature infrared spectroscopy to studies of iron substitution in tricalcium aluminate (C_3A), Cem. Concr. Res. 11 (1981) 211–218.
[136] T. Liang, Y. Nanru, Hydration products of calcium aluminoferrite in the presence of gypsum, Cem. Concr. Res. 24 (1994) 150–158.
[137] B.Z. Dilnesa, B. Lothenbach, G. Le Saout, G. Renaudin, A. Mesbah, Y. Filinchuk, A. Wichser, E. Wieland, Iron in carbonate containing AFm phases, Cem. Concr. Res. 41 (2011) 311–323.
[138] X. Yao, S. Yang, H. Dong, S. Wu, X. Liang, W. Wang, Effect of CaO content in raw material on the mineral composition of ferric-rich sulfoaluminate clinker, Constr. Build. Mater. 263 (2020) 120431.
[139] Y.-M. Kim, S.-H. Hong, H.-M. Park, Isomorphic substitution and the hydration behaviour of alinite cements, J. Eur. Ceram. Soc. 23 (2003) 2067–2073.
[140] J. Astoveza, R. Trauchessec, S. Migot-Choux, R. Soth, Y. Pontikes, Iron-rich slag addition in ternary binders of Portland cement, aluminate cement and calcium sulfate, Cem. Concr. Res. 153 (2022) 106689.
[141] N.Y. Mostafa, E.A. Kishar, S.A. Abo-El-Enein, FTIR study and cation exchange capacity of Fe^{3+}- and Mg^{2+}-substituted calcium silicate hydrates, J. Alloys Compd. 473 (2009) 538–542.
[142] L.D.S. Yadav, Raman spectroscopy, in: L.D.S. Yadav (Ed.), Organic Spectroscopy, Springer, Netherlands, Dordrecht, 2005, pp. 107–132.
[143] I.G. Richardson, J. Skibsted, L. Black, R.J. Kirkpatrick, Characterisation of cement hydrate phases by TEM, NMR and Raman spectroscopy, Adv. Cem. Res. 22 (2010) 233–248.
[144] M. Hanesch, Raman spectroscopy of iron oxides and (oxy)hydroxides at low laser power and possible applications in environmental magnetic studies, Geophys. J. Int. 177 (2009) 941–948.
[145] M. Conjeaud, H. Boyer, Some possibilities of Raman microprobe in cement chemistry, Cem. Concr. Res. 10 (1980) 61–70.
[146] P. Dariz, J. Neubauer, F. Goetz-Neunhoeffer, T. Schmid, Calcium aluminates in clinker remnants as marker phases for various types of 19th-century cement studied by Raman microspectroscopy, Eur. J. Mineral. 28 (2016) 907–914.
[147] L. Gómez-Nubla, J. Aramendia, S.F.-O. de Vallejuelo, K. Castro, J.M. Madariaga, From portable to SCA Raman devices to characterize harmful compounds contained in used black slag produced in electric arc furnace of steel industry, J. Raman Spectrosc. 44 (2013) 1163–1171.
[148] G. Renaudin, R. Segni, D. Mentel, J.-M. Nedelec, F. Leroux, C. Taviot-Gueho, A Raman study of the sulfated cement hydrates: ettringite and monosulfoaluminate, J. Adv. Concr. Technol. 5 (2007) 299–312.
[149] G. Ovcharenko, E. Ibe, A. Viktorov, Assessment of the influence of additives in concrete by the Raman spectroscopy method, E3S Web Conf. 157 (2020) 06004.
[150] N. Arrieta, A. Iturregui, I. Martinez-Arkarazo, X. Murelaga, J.I. Baceta, A. de Diego, M.A. Olazabal, J.M. Madariaga, Characterization of ferruginous cements related with weathering of slag in a temperate anthropogenic beachrock, Sci. Total Environ. 581-582 (2017) 49–65.
[151] J. Kline, B. Pesic, K. Raja, I. Ehrsam, Corrosion studies of rebar in contact with saturated solution produced by leaching of Portland type-II cement: examining the effects of chloride, carbonation and an amorphous silica additive, Corros. Eng. Sci. Technol. 53 (2018) 431–443.
[152] P. Dariz, T. Schmid, Ferruginous phases in 19th century lime and cement mortars: a Raman microspectroscopic study, Mater. Charact. 129 (2017) 9–17.
[153] B. Lafuente, R.T. Downs, H. Yang, N. Stone, The power of databases: the RRUFF project, in: T. Armbruster, R.M. Danisi (Eds.), Highlights in Mineralogical Crystallography, De Gruyter, Berlin, Germany, 2015, pp. 1–30.
[154] K. Mei, X. Cheng, T. Gu, Y. Zheng, P. Gong, B. Li, C. Zhang, L. Zhang, B. Dai, Effects of Fe and Al ions during hydrogen sulphide (H_2S)-induced corrosion of tetracalcium aluminoferrite (C_4AF) and tricalcium aluminate (C_3A), J. Hazard. Mater. 403 (2021) 123928.
[155] H. Liu, T. Chen, X. Zou, C. Qing, R.L. Frost, Effect of Al content on the structure of Al-substituted goethite: a micro-Raman spectroscopic study, J. Raman Spectrosc. 44 (2013) 1609–1614.
[156] G.W. Ward, Effect of heat treatment and cooling rate on the microscopic structure of Portland cement clinker, J. Res. Natl. Bur. Stand. 26 (1941) 49–64.
[157] D.H. Campbell, Microscopical Examination and Interpretation of Portland Cement and Clinker, Portland Cement Association, Skokie, IL, USA, 1999.
[158] P.E. Stutzman, Microscopy of clinker and hydraulic cements, Rev. Mineral. Geochem. 74 (2012) 101–146.
[159] A. Crumbie, G. Walenta, T. Füllmann, Where is the iron? Clinker microanalysis with XRD Rietveld, optical microscopy/point counting, Bogue and SEM-EDS techniques, Cem. Concr. Res. 36 (2006) 1542–1547.
[160] X. Guo, S. Yuan, Y. Xu, G. Qian, Effects of phosphorus and iron on the composition and property of Portland cement clinker utilized incinerated sewage sludge ash, Constr. Build. Mater. 341 (2022) 127754.
[161] D. Zhao, D. Zhang, W. Shen, J. Huang, X. Tang, Y. Yang, Y. Deng, Y. Wang, Investigation on industrial trial production of multi-phased clinker with crude granular steel slag, J. Clean. Prod. 337 (2022) 130467.
[162] Y. Shao, X. Lu, Q. Li, Y. Dong, L. Zhang, C. Jiang, P. Du, X. Cheng, Study on the preparation and sulfate resistance of Portland cement clinker with the high Fe/Al ratio of ferrite phase, Cem. Concr. Compos. 134 (2022) 104699.
[163] K. Scrivener, A. Bazzoni, B. Mota, J.E. Rossen, Electron microscopy, in: K. Scrivener, R. Snellings, B. Lothenbach (Eds.), A Practical Guide to Microstructural Analysis of Cementitious Materials, CRC Press, Boca Raton FL, 2016, pp. 351–417.
[164] S. Contessi, L. Calgaro, M.C. Dalconi, A. Bonetto, M.P. Bellotto, G. Ferrari, A. Marcomini, G. Artioli, Stabilization of lead contaminated soil with traditional and alternative binders, J. Hazard. Mater. 382 (2020) 120990.
[165] K. Schollbach, Q. Alam, V. Caprai, M.V.A. Florea, S.R. van der Laan, C.J.G. van Hoek, H.J.H. Brouwers, Combined characterization of the MSWI bottom ash, in: International Conference on Cement Microscopy, Lyon, France, 2016, pp. 74–82.
[166] M.I. Dominguez, J. Carpena, D. Borschnek, M.A. Centeno, J.A. Odriozola, J. Rose, Apatite and Portland/apatite composite cements obtained using a hydrothermal method for retaining heavy metals, J. Hazard. Mater. 150 (2008) 99–108.
[167] C. Rößler, B. Möser, H.-M. Ludwig, Characterization of microstructural properties of Portland cements by analytical scanning electron microscopy, in: P. Herbert (Ed.), Cementitious Materials, De Gruyter, Berlin, Boston, 2017, pp. 379–422.
[168] C. Rößler, D. Zimmer, P. Trimby, H.-M. Ludwig, Chemical – crystallographic characterisation of cement clinkers by EBSD-EDS analysis in the SEM, Cem. Concr. Res. 154 (2022) 106721.
[169] S. Ma, R. Snellings, X. Li, X. Shen, K.L. Scrivener, Alite-ye'elimite cement: synthesis and mineralogical analysis, Cem. Concr. Res. 45 (2013) 15–20.
[170] I.G. Richardson, C. Hall, G.W. Groves, TEM study of the composition of the interstitial phase in an oil-well cement clinker, Adv. Cem. Res. 5 (1993) 15–21.
[171] I.G. Richardson, The nature of the hydration products in hardened cement pastes, Cem. Concr. Compos. 22 (2000) 97–113.
[172] I.G. Richardson, G.W. Groves, Microstructure and microanalysis of hardened ordinary Portland cement pastes, J. Mater. Sci. 28 (1993) 265–277.
[173] H. Marris, K. Deboudt, P. Flament, B. Grobéty, R. Gieré, Fe and Mn oxidation states by TEM-EELS in fine-particle emissions from a Fe–Mn alloy making plant, Environ. Sci. Technol. 47 (2013) 10832–10840.
[174] B. Lanson, S. Lantenois, P.A. van Aken, A. Bauer, A. Plançon, Experimental investigation of smectite interaction with metal iron at 80 °C: structural characterization of newly formed Fe-rich phyllosilicates, Am. Mineral. 97 (2012) 864–871.
[175] A. Gloter, J. Ingrin, D. Bouchet, C. Colliex, Composition and orientation dependence of the O K and Fe $L_{2,3}$ EELS fine structures in $Ca_2(Al_xFe_{1-x})_2O_5$, Phys. Rev. B 61 (2000) 2587–2594.
[176] A. Gloter, J. Ingrin, D. Bouchet, K. Scrivener, C. Colliex, TEM evidence of perovskite–brownmillerite coexistence in the $Ca(Al_xFe_{1-x})O_{2.5}$ system with minor amounts of titanium and silicon, Phys. Chem. Miner. 27 (2000) 504–513.
[177] J. Dunn, K. Oliver, G. Nguyen, I. Sills, The quantitative determination of hydrated calcium sulphates in cement by DSC, Thermochim. Acta 121 (1987) 181–191.
[178] Y. Farnam, D. Bentz, A. Hampton, W.J. Weiss, Acoustic emission and low-temperature calorimetry study of freeze and thaw behavior in cementitious materials exposed to sodium chloride salt, Transp. Res. Rec. 2441 (2014) 81–90.
[179] J.P. Kaufmann, Experimental identification of ice formation in small concrete pores, Cem. Concr. Res. 34 (2004) 1421–1427.
[180] R. Yang, E. Lemarchand, T. Fen-Chong, A. Azouni, A micromechanics model for partial freezing in porous media, Int. J. Solids Struct. 75-76 (2015) 109–121.
[181] A. Damasceni, L. Dei, E. Fratini, F. Ridi, S.-H. Chen, P. Baglioni, A novel approach based on differential scanning calorimetry applied to the study of tricalcium silicate hydration kinetics, J. Phys. Chem. B 106 (2002) 11572–11578.
[182] E. Hoseinynezhad, F. Varaminian, The effect of sodium halide salts on the kinetics of tetrahydrofuran hydrate formation by using a differential scanning calorimetry method, J. Mol. Liq. 292 (2019) 111279.
[183] F. Ridi, L. Dei, E. Fratini, S.-H. Chen, P. Baglioni, Hydration kinetics of tri-calcium silicate in the presence of superplasticizers, J. Phys. Chem. B 107 (2003) 1056–1061.
[184] W. Sha, G.B. Pereira, Differential scanning calorimetry study of ordinary Portland cement paste containing metakaolin and theoretical approach of metakaolin activity, Cem. Concr. Compos. 23 (2001) 455–461.
[185] H. Rahier, B. Van Mele, M. Biesemans, J. Wastiels, X. Wu, Low-temperature synthesized aluminosilicate glasses, J. Mater. Sci. 31 (1996) 71–79.
[186] S.A. Bernal, M.C.G. Juenger, X. Ke, W. Matthes, B. Lothenbach, N. De Belie, J. L. Provis, Characterization of supplementary cementitious materials by thermal analysis, Mater. Struct. 50 (2016) 26.
[187] V.G. de Resende, A. Peigney, E. De Grave, C. Laurent, In situ high-temperature Mössbauer spectroscopic study of carbon nanotube–Fe–Al_2O_3 nanocomposite powder, Thermochim. Acta 494 (2009) 86–93.
[188] R.E. Vandenberghe, V.G. De Resende, G.M. Da Costa, E. De Grave, Study of loss-on-ignition anomalies found in ashes from combustion of iron-rich coal, Fuel 89 (2010) 2405–2410.
[189] J. Payá, J. Monzó, M.V. Borrachero, E. Perris, F. Amahjour, Thermogravimetric methods for determining carbon content in fly ashes, Cem. Concr. Res. 28 (1998) 675–686.
[190] R.V. Siriwardane, J.A. Poston Jr., E.P. Fisher, M.-S. Shen, A.L. Miltz, Decomposition of the sulfates of copper, iron (II), iron (III), nickel, and zinc: XPS, SEM, DRIFTS, XRD, and TGA study, Appl. Surf. Sci. 152 (1999) 219–236.
[191] G. Hu, K. Dam-Johansen, S. Wedel, J.P. Hansen, Decomposition and oxidation of pyrite, Prog. Energy Combust. Sci. 32 (2006) 295–314.
[192] R.L. Frost, Z. Ding, H.D. Ruan, Thermal analysis of goethite, J. Therm. Anal. Calorim. 71 (2003) 783–797.
[193] V.P. Ponomar, Thermomagnetic properties of the goethite transformation during high-temperature treatment, Miner. Eng. 127 (2018) 143–152.
[194] P.M.A. de Bakker, E. De Grave, R.E. Vandenberghe, L.H. Bowen, R.J. Pollard, R. M. Persoons, Mössbauer study of the thermal decomposition of lepidocrocite and characterization of the decomposition products, Phys. Chem. Miner. 18 (1991) 131–143.

[195] Y. Liu, J. Zhang, N. Bodappa, R.D.L. Smith, Mechanistic insights into lepidocrocite conversion to hematite from variable temperature Raman microscopy, J. Phys. Energy 3 (2021) 044002.
[196] U. Colombo, F. Gazzarrini, G. Lanzavecchia, G. Sironi, Magnetite oxidation: a proposed mechanism, Science 147 (1965) 1033.
[197] X. Ye, D. Lin, Z. Jiao, L. Zhang, The thermal stability of nanocrystalline maghemite, J. Phys. D. Appl. Phys. 31 (1998) 2739–2744.
[198] A. Ullrich, N. Rölle, S. Horn, From wustite to hematite: thermal transformation of differently sized iron oxide nanoparticles in air, J. Nanopart. Res. 21 (2019) 168.
[199] Y.H. Luo, D.Q. Zhu, J. Pan, X.L. Zhou, Thermal decomposition behaviour and kinetics of Xinjiang siderite ore, Miner. Process. Ext. Metall. 125 (2016) 17–25.
[200] H. Liu, Y. Wang, Y. Ma, Y. Wei, G. Pan, The microstructure of ferrihydrite and its catalytic reactivity, Chemosphere 79 (2010) 802–806.
[201] M. Ristić, E. De Grave, S. Musić, S. Popović, Z. Orehovec, Transformation of low crystalline ferrihydrite to α-Fe_2O_3 in the solid state, J. Mol. Struct. 834-836 (2007) 454–460.
[202] T. Sato, H. Fujita, T. Endo, M. Shimada, A. Tsunashima, Synthesis of hydrotalcite-like compounds and their physico-chemical properties, React. Solids 5 (1988) 219–228.
[203] G. Mie, Beiträge zur Optik trüber Medien, speziell kolloidaler Metallösungen, Ann. Phys. 330 (1908) 377–445.
[204] C.D. Gribble, A.J. Hall, A Practical Introduction to Optical Mineralogy, Springer, Dordrecht, 2012.
[205] E. Berodier, J. Bizzozero, A. Muller, Laser diffraction and gas adsorption techniques, in: K. Scrivener, R. Snellings, B. Lothenbach (Eds.), A Practical Guide to Microstructural Analysis of Cementitious Materials, CRC Press, Boca Raton FL, 2016, pp. 464–503.
[206] C.F. Ferraris, V. Hackley, A.I. Avilés, Measurement of particle size distribution in Portland cement powder: analysis of ASTM round-robin studies, Cem. Concr. Aggr. 26 (2004) CCA11920.
[207] V.A. Hackley, L.-S. Lum, V. Gintautas, C.F. Ferraris, Particle Size Distribution by Laser Diffraction Spectrometry: Application to Cementitious Powders, NIST Report NISTIR 7097, U.S. Department of Commerce, Gaithersburg MD, 2004.
[208] Y. Liu, P.H. Daum, The effect of refractive index on size distributions and light scattering coefficients derived from optical particle counters, J. Aerosol Sci. 31 (2000) 945–957.
[209] E.C. Arvaniti, M.C.G. Juenger, S.A. Bernal, J. Duchesne, L. Courard, S. Leroy, J. L. Provis, A. Klemm, N. De Belie, Physical characterization methods for supplementary cementitious materials, Mater. Struct. 48 (2015) 3675–3686.
[210] A. Zaeni, S. Bandyopadhyay, A. Yu, J. Rider, C.S. Sorrell, S. Dain, D. Blackburn, C. White, Colour control in fly ash as a combined function of particle size and chemical composition, Fuel 89 (2010) 399–404.
[211] W. Zheng, D. He, Y. Wang, J. Chen, M. Xue, H. Li, Preparation of cement-based color facing mortar by copper pyrometallurgical slag modification: efficient utilization of high-iron-content slag, J. Environ. Chem. Eng. 9 (2021) 105888.
[212] H. Song, H. Fan, H.-t. Gao, J.-a. Liu, H. Mou, Improving fly ash brightness with carbon and iron oxide removal, Recycling 5 (2020) 5.
[213] L.M. Keyte, What's Wrong With Tarong?: The Importance of Coal Fly Ash Glass Chemistry in Inorganic Polymer Synthesis, Ph.D. thesis,, University of Melbourne, 2008.
[214] B. Lothenbach, E. Wieland, A thermodynamic approach to the hydration of sulphate-resisting Portland cement, Waste Manag. 26 (2006) 706–719.
[215] L. Marjanovic, R.I. McCrindle, B.M. Botha, J.H. Potgieter, Analysis of cement by inductively coupled plasma optical emission spectrometry using slurry nebulization, J. Anal. At. Spectrom. 15 (2000) 983–985.
[216] G. Doner, A. Ege, Evaluation of digestion procedures for the determination of iron and zinc in biscuits by flame atomic absorption spectrometry, Anal. Chim. Acta 520 (2004) 217–222.
[217] T.F. Abbruzzini, C.A. Silva, D.A.d. Andrade, W.J.d.O. Carneiro, Influence of digestion methods on the recovery of iron, zinc, nickel, chromium, cadmium and lead contents in 11 organic residues, Rev. Bras. Ciênc. Solo 38 (2014) 166–176.
[218] K.I. Mahan, T.A. Foderaro, T.L. Garza, R.M. Martinez, G.A. Maroney, M. R. Trivisonno, E.M. Willging, Microwave digestion techniques in the sequential extraction of calcium, iron, chromium, manganese, lead, and zinc in sediments, Anal. Chem. 59 (1987) 938–945.
[219] A. Landajo, G. Arana, A. de Diego, N. Etxebarria, O. Zuloaga, D. Amouroux, Analysis of heavy metal distribution in superficial estuarine sediments (estuary of Bilbao, Basque Country) by open-focused microwave-assisted extraction and ICP-OES, Chemosphere 56 (2004) 1033–1041.
[220] M.J. Marqués, A. Salvador, A.E. Morales-Rubio, M. de la Guardia, Trace element determination in sediments: a comparative study between neutron activation analysis (NAA) and inductively coupled plasma-mass spectrometry (ICP-MS), Microchem. J. 65 (2000) 177–187.
[221] V. Chand, S. Prasad, ICP-OES assessment of heavy metal contamination in tropical marine sediments: a comparative study of two digestion techniques, Microchem. J. 111 (2013) 53–61.
[222] N.L. Bowen, J.F. Schairer, The system, FeO-SiO_2, Am. J. Sci. s5-24 (1932) 177–213.
[223] H.R. Shell, Determination of total iron in silicates and other nonmetallic materials, Anal. Chem. 22 (1950) 326–328.
[224] F.E. Furcas, B. Lothenbach, O.B. Isgor, S. Mundra, Z. Zhang, U.M. Angst, Solubility and speciation of iron in cementitious systems, Cem. Concr. Res. 151 (2022) 106620.
[225] P. Sarin, V. Snoeyink, D. Lytle, W. Kriven, Iron corrosion scales: model for scale growth, iron release, and colored water formation, J. Environ. Eng. 130 (2004) 364–373.
[226] S. Srivastava, R. Snellings, V. Meynen, P. Cool, Siderite-calcite ($FeCO_3$–$CaCO_3$) series cement formation by accelerated carbonation of CO_2 (g)–H_2O–Fe–$Ca(OH)_2$ systems, Cem. Concr. Compos. 122 (2021) 104137.
[227] R. Thomas, Practical Guide to ICP-MS: A Tutorial for Beginners, CRC Press, Boca Raton FL, 2008.
[228] F.G. Pinto, R.E. Junior, T.D. Saint'Pierre, Sample preparation for determination of rare earth elements in geological samples by ICP-MS: a critical review, Anal. Lett. 45 (2012) 1537–1556.
[229] S.H. Tan, G. Horlick, Matrix-effect observations in inductively coupled plasma mass spectrometry, J. Anal. At. Spectrom. 2 (1987) 745–763.
[230] J.W. Olesik, Elemental analysis using ICP-OES and ICP-MS, Anal. Chem. 63 (1991) 12A–21A.
[231] M. Murillo, Z. Benzo, E. Marcano, C. Gomez, A. Garaboto, C. Marin, Determination of copper, iron and nickel in edible oils using emulsified solutions by ICP-AES, J. Anal. At. Spectrom. 14 (1999) 815–820.
[232] L. Poirier, J. Nelson, D. Leong, L. Berhane, P. Hajdu, F. Lopez-Linares, Application of ICP-MS and ICP-OES on the determination of nickel, vanadium, iron, and calcium in petroleum crude oils via direct dilution, Energy Fuel 30 (2016) 3783–3790.
[233] T.W. May, R.H. Wiedmeyer, A table of polyatomic interferences in ICP-MS, At. Spectrosc. 19 (1998) 150–155.
[234] N. Yamada, Kinetic energy discrimination in collision/reaction cell ICP-MS: theoretical review of principles and limitations, Spectrochim. Acta B At. Spectrosc. 110 (2015) 31–44.
[235] R.E. Russo, X. Mao, J.J. Gonzalez, S.S. Mao, Femtosecond laser ablation ICP-MS, J. Anal. At. Spectrom. 17 (2002) 1072–1075.
[236] F.-X. d'Abzac, A.D. Czaja, B.L. Beard, J.J. Schauer, C.M. Johnson, Iron distribution in size-resolved aerosols generated by UV-femtosecond laser ablation: influence of cell geometry and implications for in situ isotopic determination by LA-MC-ICP-MS, Geostand. Geoanal. Res. 38 (2014) 293–309.
[237] M. Cruz-Alonso, B. Fernandez, A. Navarro, S. Junceda, A. Astudillo, R. Pereiro, Laser ablation ICP-MS for simultaneous quantitative imaging of iron and ferroportin in hippocampus of human brain tissues with Alzheimer's disease, Talanta 197 (2019) 413–421.
[238] F. Kleiner, M. Decker, C. Rößler, H. Hilbig, H.-M. Ludwig, Combined LA-ICP-MS and SEM-EDX analyses for spatially resolved major, minor and trace element detection in cement clinker phases, Cem. Concr. Res. 159 (2022) 106875.
[239] M. Bonta, A. Eitzenberger, S. Burtscher, A. Limbeck, Quantification of chloride in concrete samples using LA-ICP-MS, Cem. Concr. Res. 86 (2016) 78–84.
[240] B. Huber, H. Hilbig, M.M. Mago, J.E. Drewes, E. Müller, Comparative analysis of biogenic and chemical sulfuric acid attack on hardened cement paste using laser ablation-ICP-MS, Cem. Concr. Res. 87 (2016) 14–21.
[241] J. Willis, Nitrous oxide–acetylene flame in atomic absorption spectroscopy, Nature 207 (1965) 715–716.
[242] L. Capacho-Delgado, D.C. Manning, The determination by atomic-absorption spectroscopy of several elements, including silicon, aluminium and titanium, in cement, Analyst 92 (1967) 553–557.
[243] G. Tyler, ICP-OES, ICP-MS and AAS Techniques Compared, ICP Optical Emission Spectroscopy Technical Note 5, Horiba Group, Longjumeau, France, 1995.
[244] S. Panda, P. Sarkar, Leaching behavior of copper slag aggregate cement-mortar by atomic absorption spectroscopy (AAS), Mater. Today Proc. 33 (2020) 5123–5129.
[245] K. Andersson, B. Allard, M. Bengtsson, B. Magnusson, Chemical composition of cement pore solutions, Cem. Concr. Res. 19 (1989) 327–332.
[246] W.F. Hillebrand, G.E.F. Lundell, Applied Inorganic Analysis: With Special Reference to the Analysis of Metals, Minerals and Rocks, Wiley, New York, 1929.
[247] J.H. Pratt, On the determination of ferrous iron in silicates, Am. J. Sci. s3-48 (1894) 149–151.
[248] W.R. Crowell, W.W. Luke, T.G. Mastin, Determination of iron by the Zimmerman-Reinhardt method, Ind. Eng. Chem. Anal. Ed. 13 (1941) 94–95.
[249] L. Kampf, Volumetric determination of iron and aluminum in cement with 8-Hydroxyquinoline, Ind. Eng. Chem. Anal. Ed. 13 (1941) 72–73.
[250] C. Lucchesi, C. Hirn, EDTA titration of total iron in iron (ii) and iron (iii) mixtures. Application to iron driers, Anal. Chem. 32 (1960) 1191–1193.
[251] ASTM International, ASTM C114-22: Standard Test Methods for Chemical Analysis of Hydraulic Cement, West Conshohocken PA, 2022.
[252] R. Gill, Modern Analytical Geochemistry: An Introduction to Quantitative Chemical Analysis Techniques for Earth, Environmental and Materials Scientists, Routledge, New York NY, 2014.
[253] CEN, EN 196-2:2013, Method of Testing Cement - Chemical Analysis of Cement, Brussels, 2013.
[254] J. Van De Sande, A. Peys, T. Hertel, H. Rahier, Y. Pontikes, Upcycling of non-ferrous metallurgy slags: identifying the most reactive slag for inorganic polymer construction materials, Resour. Conserv. Recycl. 154 (2020) 104627.
[255] A. Beer, Bestimmung der Absorption des rothen Lichts in farbigen Flüssigkeiten, Ann. Phys. 162 (1852) 78–88.
[256] A.E. Harvey Jr., J.A. Smart, E.S. Amis, Simultaneous spectrophotometric determination of iron (II) and total iron with 1,10-phenanthroline, Anal. Chem. 27 (1955) 26–29.
[257] R. Bastian, R. Weberling, F. Palilla, Determination of Iron by ultraviolet spectrophotometry, Anal. Chem. 28 (1956) 459–462.
[258] F. Cheng, T. Zhang, C. Yang, H. Zhu, Y. Li, T. Sun, C. Zhou, A direct and rapid method for determination of total iron in environmental samples and hydrometallurgy using UV–vis spectrophotometry, Microchem. J. 179 (2022) 107478.
[259] L.L. Stookey, Ferrozine - a new spectrophotometric reagent for iron, Anal. Chem. 42 (1970) 779–781.

[260] A. Mancini, E. Wieland, G. Geng, B. Lothenbach, B. Wehrli, R. Dähn, Fe(II) interaction with cement phases: method development, wet chemical studies and X-ray absorption spectroscopy, J. Colloid Interface Sci. 588 (2021) 692–704.
[261] J.S. Fritz, Ion chromatography, Anal. Chem. 59 (1987) 335A–344A.
[262] J. Weiss, Detection methods in ion chromatography, in: J. Weiss (Ed.), Handbook of Ion Chromatography, Wiley-VCH Verlag, Weinheim, 2016, pp. 731–810.
[263] Y. Noguchi, L. Zhang, T. Maruta, T. Yamane, N. Kiba, Simultaneous determination of fluorine, chlorine and bromine in cement with ion chromatography after pyrolysis, Anal. Chim. Acta 640 (2009) 106–109.
[264] M. Poznic, R. Gabrovsek, M. Novic, Ion chromatography determination of chloride and sulphate in cement, Cem. Concr. Res. 29 (1999) 441–443.
[265] M. Balonis, B. Lothenbach, G. Le Saout, F.P. Glasser, Impact of chloride on the mineralogy of hydrated Portland cement systems, Cem. Concr. Res. 40 (2010) 1009–1022.
[266] Y. Kanai, Simultaneous determination of iron(II) and iron(III) oxides in geological materials by ion chromatography, Analyst 115 (1990) 809–812.
[267] S. Schnell, S. Ratering, K.-H. Jansen, Simultaneous determination of iron (III), iron (II), and manganese (II) in environmental samples by ion chromatography, Environ. Sci. Technol. 32 (1998) 1530–1537.
[268] M. Fredrikson, N.-G. Carlsson, A. Almgren, A.-S. Sandberg, Simultaneous and sensitive analysis of Cu, Ni, Zn, Co, Mn, and Fe in food and biological samples by ion chromatography, J. Agric. Food Chem. 50 (2002) 59–65.
[269] M. Jiang, C. Rößler, E. Wellmann, J. Klaver, F. Kleiner, J. Schmatz, Workflow for high-resolution phase segmentation of cement clinker from combined BSE image and EDX spectral data, J. Microsc. 286 (2022) 85–91.
[270] P. Teck, R. Snellings, J. Elsen, Method for quantifying the reaction degree of slag in alkali-activated cements using deep learning-based electron microscopy image analysis, J. Microsc. 286 (2022) 174–178.